Sanmiguel Vila, C., Vinuesa, R., Discetti, S., Ianiro, A., Schlatter, P. y Örlü, R. (2017). On the identification of well-behaved turbulent boundary layers. *Journal of Fluid Mechanics*, 822, pp. 109 - 138.

DOI: https://doi.org/10.1017/jfm.2017.258

On the identification of well-behaved turbulent boundary layers

C. Sanmiguel Vila[1], R. Vinuesa[2], S. Discetti[1], A. Ianiro[1], P. Schlatter[2] and R. Örlü[2]†

[1] Aerospace Engineering Group, Universidad Carlos III de Madrid, Leganés, Spain.
[2] Linné FLOW Centre, KTH Mechanics, SE-100 44 Stockholm, Sweden.

The present paper introduces a new method based on the diagnostic plot (Alfredsson *et al.*, Phys. Fluids, **23**:041702, 2011) to assess the convergence towards a well-behaved zero-pressure-gradient (ZPG) turbulent-boundary layer (TBL). The most popular and well understood methods to assess the convergence towards a well-behaved state rely on empirical skin-friction curves (requiring accurate skin-friction measurements), shape-factor curves (requiring full velocity profile measurements with an accurate wall position determination) or wake-parameter curves (requiring both of the previous quantities). On the other hand, the proposed diagnostic-plot method only needs measurements of mean and fluctuating velocities in the outer region of the boundary layer at arbitrary wall-normal positions. To test the method, six tripping configurations, including optimal setups as well as both under and over-tripped cases, are used to quantify the convergence of zero-pressure-gradient turbulent boundary layers towards well-behaved conditions in the Reynolds-number range covered by recent high-fidelity direct-numerical simulation (DNS) data up to a Re_θ of around 4,000 (corresponding up to 2.5 m from the leading edge). Additionally, recent high Re data sets have been employed to validate the method. Results show that weak tripping configurations lead to deviations in the mean flow and the velocity fluctuations within the logarithmic region with respect to optimally-tripped boundary layers. On the other hand, a strong trip leads to a more energized outer region, manifested in the emergence of an outer peak in the velocity-fluctuation profile and in a more prominent wake region. While established criteria based on skin-friction and shape-factor correlations yield generally equivalent results with the diagnostic-plot method in terms of convergence towards a well-behaved state, the proposed method has the advantage of being a practical surrogate that is a more efficient tool when designing the set-up for TBL experiments, since it diagnoses the state of the boundary layer without the need to perform extensive velocity profile measurements.

Key words: Turbulent boundary layers, turbulent flows

1. Introduction

Turbulent boundary layers (TBLs) are of paramount importance given their ubiquitous presence in many relevant fluid-flow problems such as the flow over wings, land and sea vehicles, turbines, compressors, etc. Due to the complex physics present in these flows, simplified scenarios such as the zero pressure gradient (ZPG) TBL developing over

† Email address for correspondence: ramis@mech.kth.se

a flat plate are investigated to understand the fundamental aspects of wall-bounded turbulence. In experimental ZPG TBL studies, the transition to turbulence of a laminar boundary layer is commonly induced using an external perturbation, since natural transition requires long development lengths, and is significantly affected by external disturbances (Tani 1969). The perturbation used to trigger transition in experimental studies is typically a trip (Klebanoff & Diehl 1954; Erm & Joubert 1991), and it is important to carefully design it, in accordance with the inflow conditions, since an inadequate choice of this perturbation may condition the results of the study (Hutchins 2012). Effects such as inflow conditions, tripping devices and development length, which may lead to local non-equilibrium conditions producing flows that are no longer representative of the *canonical* ZPG TBL, have started to receive some renewed attention in recent years. Consequently, criteria and methods to determine if a TBL can be considered as *well-behaved*, (*i.e.*, not in a post-transitional state or affected by non-equilibrium effects), have been the object of increasing interest. In the context of this study, the term *well-behaved* refers to a state in which the TBL is independent of the tripping conditions and flow history, as defined in the work by Chauhan *et al.* (2009). In particular, the well-behaved state corresponds to that of a canonical ZPG TBL, which is a particular case of near-equilibrium boundary layer in which the mean velocity defect is self-similar in the outer region at high Reynolds numbers as discussed for instance by Marusic *et al.* (2010).

A number of different trip devices, including wires, distributed grit and cylindrical pins, were studied by Erm & Joubert (1991) in the Reynolds number range $715 \leqslant Re_\theta \leqslant 2,815$, where the subscript θ denotes the momentum thickness. In their work, Erm & Joubert (1991) designed the trip devices to obtain a correct stimulation of the flow at a specific velocity, adapting the trip height iteratively until the measured value of ΔU^+ (proportional to the so-called wake parameter Π), which is the maximum deviation of a given profile from the logarithmic law, would agree with the empirical relation between ΔU^+ and Re_θ proposed by Coles (1962). Note that in the present study the superscript '+' denotes scaling with the friction velocity u_τ and the viscous length $\ell_* = \nu/u_\tau$ (where $u_\tau = \sqrt{\tau_w/\rho}$, τ_w, being the mean wall-shear stress, ρ the fluid density and ν the kinematic viscosity). Additionally, Erm & Joubert (1991) have shown that for varying free-stream velocities the ΔU^+ versus Re_θ curves would not agree with the one proposed by Coles (1962, 1968) at Reynolds numbers below $Re_\theta \simeq 3,000$, which manifests the flow sensitivity to the particular tripping device, especially at early development stages. Moreover, when the flow is not properly stimulated, the initial evolution of parameters such as the shape factor $H = \delta^*/\theta$ (where δ^* is the displacement thickness) and the skin friction coefficient $C_f = 2\tau_w/\left(\rho U_\infty^2\right)$ (where U_∞ is the free-stream velocity) may differ in the low-Re range below $Re_\theta \simeq 3,000$. In this context, Castillo & Johansson (2002) studied the effect of the upstream conditions on low Reynolds number ZPG TBLs by varying the wind tunnel speed while maintaining the trip wire size and its location. They reported that the evolution of parameters such as the growth rate of the boundary layer or the Reynolds shear stresses were affected by the different inflow conditions. The fact that the upstream conditions play such an important role in the downstream flow implies that experiments with the same local Reynolds number may produce different results depending on the particular tripping strategy adopted. As a consequence, discrepancies between different experimental studies can be found in the literature. In order to discern which ZPG TBL can be considered *"well-behaved"*, Chauhan *et al.* (2009), taking up the seminal works by Coles (1968) and Fernholz & Finley (1996), analyzed and compared in detail a large number of experimental databases with significant discrepancies among them. They fitted a wide range of velocity profiles to a composite profile formulation (Chauhan *et al.* 2009) in order to obtain the wake parameter Π (Coles 1956) and the shape

factor H, besides the skin-friction coefficient. By comparing the streamwise evolution of the measured values of C_f, H and Π with respect to the ones predicted through numerical integration of the composite profile, Chauhan *et al.* (2009) identified *well-behaved* profiles.

Marusic *et al.* (2015) further investigated on the evolution of ZPG TBLs tripped with different tripping devices. In their study the trip strength was varied in an incremental fashion from weak tripping up to over-tripping with all other parameters kept constant, including local Reynolds number, pressure-gradient conditions, etc. The aim of their work was to compare TBL evolutions from various tripping configurations at matched local Reynolds numbers. The trip strength was modified by considering a standard sandpaper trip, together with two threaded rods of different diameters designed to overstimulate the boundary layer. They reported the evolution of the different flows until their equilibrium state, and observed that the effects of the particular trip persisted up to streamwise distances of the order of $2,000$ trip heights. However, this conclusion is only valid for their particular setup and trip method. The trip effects were especially evident on the large-scale motions (residing in the outer layer) in the flow, which are effectively energized by the overstimulating tripping configurations.

With the aim of generating canonical high-Reynolds number TBLs in short wind tunnels, a study of tripping configurations was carried out by Rodríguez-López *et al.* (2016). A sawtooth serrated fence and different spanwise arrays of cylinders were employed to obtain a uniform wall-normal blockage distribution case and a non-uniform one. In their study, Rodríguez-López *et al.* (2016) have shown how tripping configurations with a uniform blockage ratio can be used to obtain canonical high-Reynolds number TBLs with an increase of up to 150% in momentum thickness with respect to a standard sandpaper trip. It was also shown that, after an adaptation region, tripping configurations with uniform blockage ratio eventually lead to a canonical state in contrast with configurations with non-uniform blockage ratio, which do not generate canonical TBLs even after a long recovery distance.

The choice of tripping strategy and inflow conditions also affects significantly the results from numerical simulations, as shown by Schlatter & Örlü (2010). Their results shown that the impact of transitional effects through the boundary layer development and the slow convergence of the outer layer can lead to important differences, as shown through the comparison of a wide number of direct numerical numerical simulation (DNS) databases of ZPG TBLs. The estimated values of parameters such as H and C_f may differ up to 5% and 20%, respectively. In a follow-up study, Schlatter & Örlü (2012) reported that if transition is initiated at Reynolds numbers based on momentum thickness $Re_\theta < 300$, then comparisons between different numerical and experimental databases can be made for $Re_\theta > 2,000$ if the flow is not over or under-tripped. Thus, under these conditions the ZPG TBL can be considered as *canonical*, and does not exhibit features reminiscent of its particular inflow condition. Along the lines of these studies, the importance of selecting an adequate trip condition for producing a canonical TBL was highlighted by Hutchins (2012).

Whereas Schlatter & Örlü (2012) considered a laminar boundary layer as inflow for their simulations, and used a tripping method based on wall-normal volume forcing which emulates the effect of experimental tripping devices, Sillero *et al.* (2013) used a recycling method based on the one proposed by Lund *et al.* (1998) to generate synthetic inflow conditions for their DNS of a ZPG TBL. Simens *et al.* (2009) suggested that when considering synthetic inflow conditions, the turnover length may be a better measure than Re_θ of how quickly the boundary layers recover from a specific inflow condition.

The turnover length $\tilde{x}$ is the distance the eddies are advected during a turnover time δ/u_τ (δ being the boundary-layer thickness), as defined through:

$$\tilde{x} = \int^x \mathrm{d}x / \left(\delta U_\infty^+\right), \tag{1.1}$$

where x is the streamwise coordinate. Sillero *et al.* (2013) reported that in their simulations the parameters connected to the small scales, such as the maximum Reynolds stress, require a recovery distance of $\tilde{x} \simeq 1$. The variables connected to the larger scales, on the other hand, require longer recovery distances (in agreement with the observations by Schlatter & Örlü 2012), *viz.* as much as $\tilde{x} \simeq 3-4$ in the case of H or δ/θ, and $\tilde{x} \simeq 4-5$ for Π. Note that this may lead to the fact that the computational domain is not long enough to allow full development of the large-scale motions in the TBL, as it was the case in one of the preliminary simulations reported by Sillero *et al.* (2013).

In another recent study, Kozul *et al.* (2016) studied a temporally-developing turbulent boundary layer through DNS, in a setup where the lower plate is suddenly set into motion, as in the case of TBLs developing on a flat plate in towing-tank experiments (Lee *et al.* 2014). The initial velocity profile they used is similar to that of the wake after a wall-mounted trip wire used in wind tunnels. They also assessed how different trip conditions affected the results in terms of a "trip Reynolds number" based on the trip-wire diameter. In their study it is shown that as the ratio of momentum thickness to trip-wire diameter approaches unity, the flow converges towards a state free from the effects of its starting trip Reynolds number. This is an interesting conclusion due to the connection between experimental trip devices, and numerical characterization of temporally-developing TBLs.

In the present study the primary objective is to investigate whether there exists a criterion to identify a well-behaved boundary layer for both experiments and simulations without the need of acquiring huge amount of data and without relying on quantities difficult to be measured (such as the wall distance or the wall shear stress). The present investigation revisits the early experimental studies on the history effects of tripping devices on turbulence characteristics at low Re (see *e.g.* Erm & Joubert 1991) in light of the recent numerical as well as high Re experimental studies with the aim to a) assess the various criteria proposed in the literature to discern a *canonical* ZPG TBL and b) propose a practical method that can be employed prior to extensive measurements and/or DNS.

The article is organized as follows: the experimental setup is described in §2, upon which the boundary-layer development from the various inflow conditions are compared and presented in §3. A method to assess the boundary-layer development based on the diagnostic-plot method (Alfredsson *et al.* 2011) is presented in §4, and its outcomes are compared with those of other available criteria. Prior to the summary and conclusions in §5, the proposed method is demonstrated to be a practically feasible and efficient tool when designing the set-up for TBL experiments.

2. Experimental set-up

2.1. *Wind tunnel and boundary-layer flow conditions*

Experiments were carried out in the *Minimum Turbulence Level* (MTL) closed-loop wind tunnel located at KTH Royal Institute of Technology in Stockholm. The test section is 7 m long with a cross-sectional area of 0.8×1.2 m^2 (height $\times$ width). This tunnel is capable of reaching a maximum speed of 70 m/s with a streamwise velocity disturbance level of approximately 0.025% of the free-stream velocity at a test speed of 25 m/s.

Tripping case	Characteristics and location	Color code	Description
①	DYMO "V" at $x = 75$ mm	Red	Weak tripping
②	DYMO "V" at $x = 75$, 90, 115 mm and 5 mm square bar at $x = 85$ mm	Black	Strong over-tripping
③	DYMO "V" at $x = 90$, 115 mm and 2.4 mm height turbulator	Blue	Optimal tripping 1
④	DYMO "V" at $x = 90$, 115 mm and 1.6 mm height turbulator	Magenta	Optimal tripping 2
⑤	DYMO "V" at $x = 90$ mm	Green	Weak, late tripping
⑥	DYMO "V" at $x = 230$ mm	Brown	Weak, very late tripping

TABLE 1. Specifications of the tripping configurations including location and respective color coding for symbols. The embossed (DYMO) letter "V" points downstream and has a nominal height of 0.3 mm.

The air temperature can be controlled with an accuracy of ± 0.05°C by means of a heat exchanger. More details on the MTL can be found in Lindgren & Johansson (2002). Measurements of the turbulent boundary layer developing over the flat plate were performed at a nominal free-stream velocity of 12 m/s. The aluminum flat plate of 6 m length and 26 mm thickness, spanned the entire width of the wind tunnel and was suspended 25 cm above the tunnel floor. The flat plate has a leading edge following the shape of a modified super ellipse and is equipped with a trailing-edge flap plate to modify the position of the stagnation point on the leading edge. For a more detailed description the reader is referred to Österlund (1999).

The boundary layer was tripped close to the leading edge with a set of tripping devices in order to obtain a range of different tripping conditions. Using as a reference the cases studied numerically by Schlatter & Örlü (2012), a combination of weak, late, optimal and strong trippings were tested. In this study, the nomenclature *optimal* is referred to cases in which the boundary layer is neither overstimulated nor underestimulated by the tripping and that the profiles would lead to a common state within the streamwise distance considered here. With this aim, *DYMO* tapes (with the embossed letter 'V' pointing in the flow direction and a nominal height of 0.3 mm) in various combinations with and without turbulators were used to establish 5 different initial evolutions of the TBL. Additionally, a square bar with a side length of 5 mm was used to obtain a strongly over-tripped case. The 6 different tripping cases under consideration are summarized in Table 1, which also reports the color coding used for such tripping condition, through the remainder of the paper, and represented in Figure 1. All the tripping configurations were placed spanning the full spanwise length of the plate and at a streamwise location in the range $75 < x\,[\text{mm}] < 230$ from the leading edge, corresponding to the range $130 < Re_\theta < 260$ in terms of the laminar boundary layer as can be observed in Figure 1.

An initial set of 4 streamwise locations were selected for measurements on each tripping configuration. Additional stations were added to match Re_θ, covering a final Reynolds number range of $440 < Re_\theta < 4,070$ as shown in Table 3. The streamwise pressure-gradient distribution was controlled by adjusting the wind tunnel ceiling, which comprises a total of six panels allowing vertical displacement. The evolution of the pressure coefficient C_p from the leading edge ($x = 0$ m) down to $x = 3.5$ m is shown in Figure 2 for the 6 tripping cases under consideration, as well as for an additional case where no tripping was used (and where the boundary layer remained laminar). This figure shows

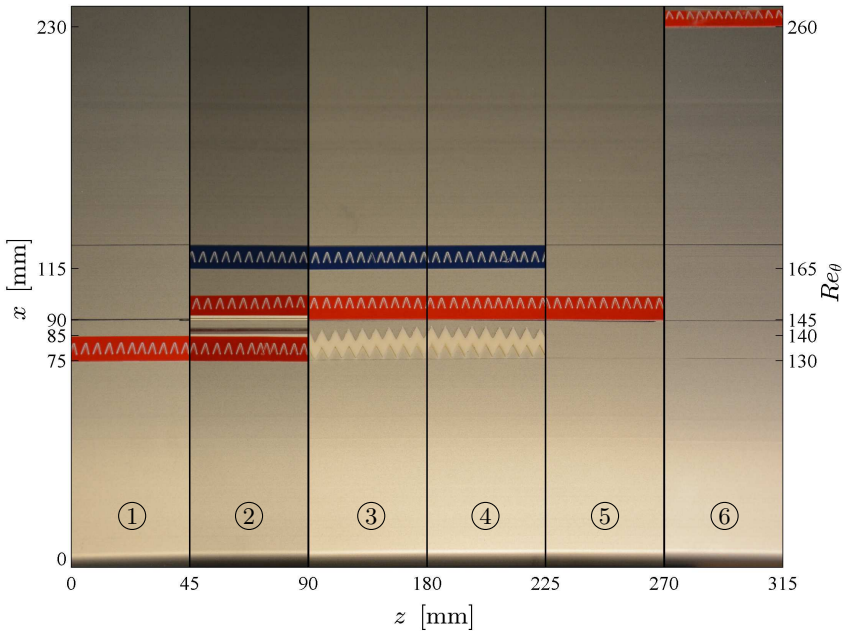

FIGURE 1. Schematic view of the tripping configurations used in the present study and summarized in Table 1, with streamwise direction from bottom to top. The indicated momentum-thickness Reynolds number Re_θ is related to the laminar boundary layer in absence of the trip. Note that the difference between ③ and ④ is the height of the turbulator, and is hence not visible in the present two-dimensional view. The scale in mm is included in order to provide a reference for the size of the "V" and the turbulator pattern.

the quality of the ZPG established in the test section, with C_p values between -0.01 and 0.01, and deviations in U_∞ below 0.5%, which is comparable in quality with related studies, see *e.g.* Marusic *et al.* (2015). From Figure 2 it can be observed that the changes in displacement thickness δ^* due to the different tripping configurations have a very small influence in the pressure distribution. This is due to the large ratio between the distance from the flat plate and the tunnel ceiling (around 0.55 m), and the maximum displacement thickness, which is below around 1%.

2.2. *Hot-wire anemometry measurements*

Streamwise velocity measurements were performed by means of a home-made single hot-wire probe resembling a standard *Dantec* boundary-layer probe, *i.e.*, a 55P15. The hot-wire probe was etched in-house using a stubless Platinum wire of 560 μm length and nominal diameter of 2.5 μm, which was soldered to conical prongs with diameter of around 30 μm. Voltage signals from the hot-wire were recorded using a *Dantec StreamLine* 90N10 frame in conjunction with a 90C10 constant-temperature anemometer module operated at a resistance overheat ratio of 80%. An offset and gain were applied to the top-of-the-bridge voltage in order to match the voltage range of the 16-bit A/D converter used. All the measurements were recorded using a sampling frequency of 20 kHz and acquisition time of 30 s, and a low-pass filter of 10 kHz cut-off frequency was used prior to the data acquisition in order to avoid aliasing. Calibration of the hot-wire was performed in situ using as reference a Prandtl tube located parallel to the incoming free stream. The Prandtl tube was connected to a micromanometer of type *FC0510 (Furness*

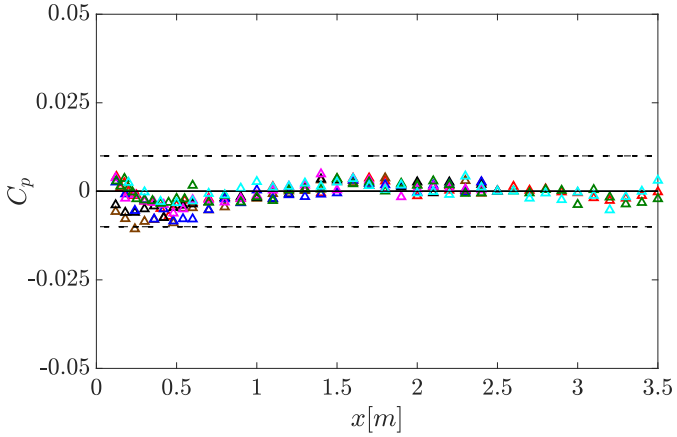

FIGURE 2. Streamwise variation of the pressure coefficient C_p for the 6 tripping configurations considered in the present study. See Table 1 for the used color code. The additional cyan symbols correspond to a case in which no tripping was used. Reference dash lines at $C_p = \pm 0.010$ are included.

Control Limited), which was also employed to record the ambient temperature and pressure during the calibration and the experiments. Data acquired in the calibration was fitted to a fourth-order polynomial curve, which is a rather common procedure in the wall-turbulence community (see *e.g.* Morrison *et al.* 2004; Hultmark *et al.* 2010). Hot-wire measurements were acquired with a sufficiently large number of points within the sublayer and buffer region in order to correct for the absolute wall position and determine the friction velocity (Örlü & Vinuesa 2017) without relying on log-law constants. The composite profile given by Chauhan *et al.* (2009) is used to fit the experimental data and correct the absolute wall position as well as to obtain the friction velocity, which has been shown to be a robust method whenever near-wall measurements are at hand (Örlü *et al.* 2010; Rodríguez-López *et al.* 2015). Additional oil-film interferometry measurements, described in §2.3, were performed for some selected conditions and were utilized to validate the aforementioned procedure to determine the friction velocity. The experimental uncertainties associated with the measurements were determined through an approach based on a Monte Carlo simulation, assuming random errors in the velocity measurements, viscosity and absolute wall position with the following uncertainties: 1%, 0.2% and 15 μm, respectively (see *e.g.* Bailey *et al.* 2013). A summary of the resulting uncertainties is shown in Table 2.

2.3. *Oil-film interferometry measurements*

Oil-film interferometry (OFI) was used to measure the wall-shear stress, and validate the process to determine the friction velocity based on near-wall velocity measurements described in §2.2. To this end, the OFI measurements were carried out a the same positions as the hot-wire. Silicon oil with a nominal viscosity of 200 cSt at 25°C was used. The oil viscosity was calibrated by means of a capillary-suspended level viscometer. Black Mylar films were attached to the flat plate in order to obtain better contrast for the fringe patterns from the oil-film light reflections. The oil film was illuminated using a low-pressure sodium lamp which had a power of 55 W and a nominal wavelength of 589 nm and was placed on the wind tunnel roof. A handhold digital thermocouple *Fluke* was attached to the flat plate close to the recording station to control the oil temperature. The equipment used to obtain the pictures consisted of a digital single-lens reflex camera *Nikon*

Quantity	Notation	Uncertainty (±)
Temperature	T	0.2%
Dynamic pressure	Δp	0.4%
Atmospheric pressure	p_∞	0.1%
Air density	ρ	0.2%
Kinematic viscosity	ν	0.2%
Velocity	U	1.0%
Wall position	Δy	15 μm
Friction velocity	u_τ	0.8%
Momentum thickness	θ	0.5%
Displacement thickness	δ^*	0.5%
Wake parameter	Π	2.5%

TABLE 2. Uncertainty estimates for various measured quantities.

D7100, and telephoto zoom lens *Nikon Nikkor 200 mm f4*. The camera was placed on the roof of the wind tunnel with an angle of 15° normal to the plate, and was controlled remotely via a USB cable. For further details on the performed oil-film interferometry measurements, as well as on the post-processing of the data, the reader is referred to Örlü & Schlatter (2013) and Vinuesa & Örlü (2017), respectively. Also note that we do not expect the very small local pressure gradient observed at around $x \simeq 0.4$ m in Figure 2 to impact the OFI results, since this technique has been used in other studies dealing with pressure-gradient TBLs (Monty *et al.* 2011*a*; Vinuesa *et al.* 2014), where no effects that would produce a significant bias were observed.

3. TBL evolution for various tripping configurations

In this section, we analyze streamwise mean velocity and velocity fluctuation profiles, as well as spectra, to assess the evolution of the TBL from the various tripping devices described in Table 1. All the velocity profiles under consideration are summarized in Table 3, where, following the procedure proposed by Schlatter & Örlü (2010), the composite profile by Nickels (2004) was used to obtain the free-stream velocity U_∞ and the 99% boundary-layer thickness δ_{99} in a consistent manner, upon which the Reynolds numbers, integral quantities and boundary layer parameters were then computed. The summary in this table will also serve as an identification sheet for the data sets made available with this paper. As shown in Table 3, all the velocity profiles were measured in the range $0.24 < x$ [m] < 2.5 from the flat-plate leading edge. In terms of spatial resolution, the hot-wire probe length can be considered nominally matched in terms of viscous length to approximately 20, while the temporal resolution is as well sufficiently well-resolved based on the criteria set by Hutchins *et al.* (2009, 2015).

3.1. *Comparison of TBLs at the same streamwise location*

Mean streamwise velocity and velocity fluctuation profiles are shown at four streamwise measuring stations, for the six tripping cases, in Figure 3. For the tripping configurations from ① to ⑤, the near-wall region collapses in all the stations, in agreement with the conclusions from Schlatter & Örlü (2012) who showed that this region is expected to adapt quickly to a canonical TBL development. Interestingly, case ⑥ (weak, very late trip; subplot k)) in which the tripping is located at $x = 0.23$ m, corresponding to $Re_\theta =$

Case	x [m]	Re_θ	Re_τ	u_τ [m/s]	δ_{99} [mm]	θ [mm]	δ^* [mm]	H	Π	ν/u_τ [μm]	L^+	Δt^+	TU_∞/δ_{99}
① Weak	**0.24**	540	210	0.58	5.82	0.69	1.09	1.59	0.38	26.2	21	1.11	61,800
① Weak	**0.60**	1,200	430	0.53	13.09	1.52	2.23	1.47	0.37	28.4	20	0.94	27,500
① Weak	**1.10**	1,950	650	0.50	19.81	2.48	3.56	1.44	0.44	30.5	18	0.82	18,100
① Weak	**1.80**	2,900	910	0.47	28.68	3.70	5.25	1.42	0.55	32.4	17	0.72	12,400
② Strong	**0.24**	1,770	620	0.53	20.96	2.25	3.17	1.41	-0.03	28.4	20	0.93	17,000
② Strong	**0.60**	2,330	1,120	0.52	31.45	2.96	3.90	1.32	-0.21	28.8	19	0.91	11,300
② Strong	**1.10**	3,040	1,240	0.49	36.53	3.86	5.17	1.34	0.09	30.5	18	0.81	9,700
② Strong	**1.80**	4,070	1,390	0.46	51.13	5.20	7.03	1.35	0.35	32.6	17	0.71	6,900
③ Optimal 1	**0.24**	1,030	420	0.55	11.39	1.32	1.91	1.45	0.12	27.3	21	1.01	31,100
③ Optimal 1	**0.60**	1,600	580	0.51	16.74	2.03	2.90	1.43	0.31	29.3	19	0.88	21,200
③ Optimal 1	0.90	2,040	690	0.49	22.47	2.60	3.70	1.42	0.40	30.5	18	0.81	15,700
③ Optimal 1	**1.10**	2,340	760	0.48	24.81	2.98	4.24	1.42	0.46	31.2	18	0.78	14,300
③ Optimal 1	**1.80**	3,290	1,000	0.46	35.94	4.19	5.91	1.41	0.45	32.6	17	0.71	9,900
④ Optimal 2	**0.24**	700	300	0.58	7.87	0.89	1.33	1.49	0.09	25.8	22	1.12	45,200
④ Optimal 2	**0.60**	1,360	490	0.52	13.90	1.72	2.49	1.45	0.31	28.7	20	0.91	25,600
④ Optimal 2	0.95	1,910	640	0.49	18.68	2.42	3.48	1.44	0.46	30.3	18	0.82	19,100
④ Optimal 2	**1.10**	2,140	700	0.49	22.47	2.71	3.88	1.43	0.44	30.7	18	0.80	15,800
④ Optimal 2	**1.80**	3,090	960	0.46	30.31	3.92	5.56	1.42	0.55	32.3	17	0.72	11,700
⑤ Weak, late	**0.24**	440	190	0.61	4.60	0.55	0.87	1.59	0.24	24.6	23	0.41	78,100
⑤ Weak, late	**0.60**	1,190	410	0.52	12.04	1.48	2.21	1.49	0.45	28.5	20	0.31	29,800
⑤ Weak, late	**1.10**	1,950	630	0.49	20.61	2.44	3.53	1.44	0.51	30.4	18	0.27	17,400
⑤ Weak, late	**1.80**	2,900	910	0.47	30.44	3.64	5.16	1.42	0.52	31.7	18	0.25	11,800
⑥ Weak, very late	**0.60**	480	70	0.24	4.10	0.60	1.24	2.06	0.0	62.3	9	0.19	87,000
⑥ Weak, very late	**1.10**	600	90	0.22	6.33	0.76	1.54	2.03	0.0	68.8	8	0.16	56,300
⑥ Weak, very late	**1.80**	1,440	520	0.52	17.27	1.82	2.62	1.43	0.35	29	19	0.89	20,600
⑥ Weak, very late	2.10	1,930	680	0.50	21.87	2.48	3.51	1.41	0.29	30.2	19	0.83	16,000
⑥ Weak, very late	2.50	2,500	830	0.48	30.23	3.22	4.51	1.40	0.37	31.3	18	0.77	11,600

TABLE 3. Experimental parameters for all the profiles in the present study. The measurement stations x that are common to all the trip configurations are highlighted in bold. The hot-wire length is denoted by L, Δt is the time between samples and T is the total sampling time.

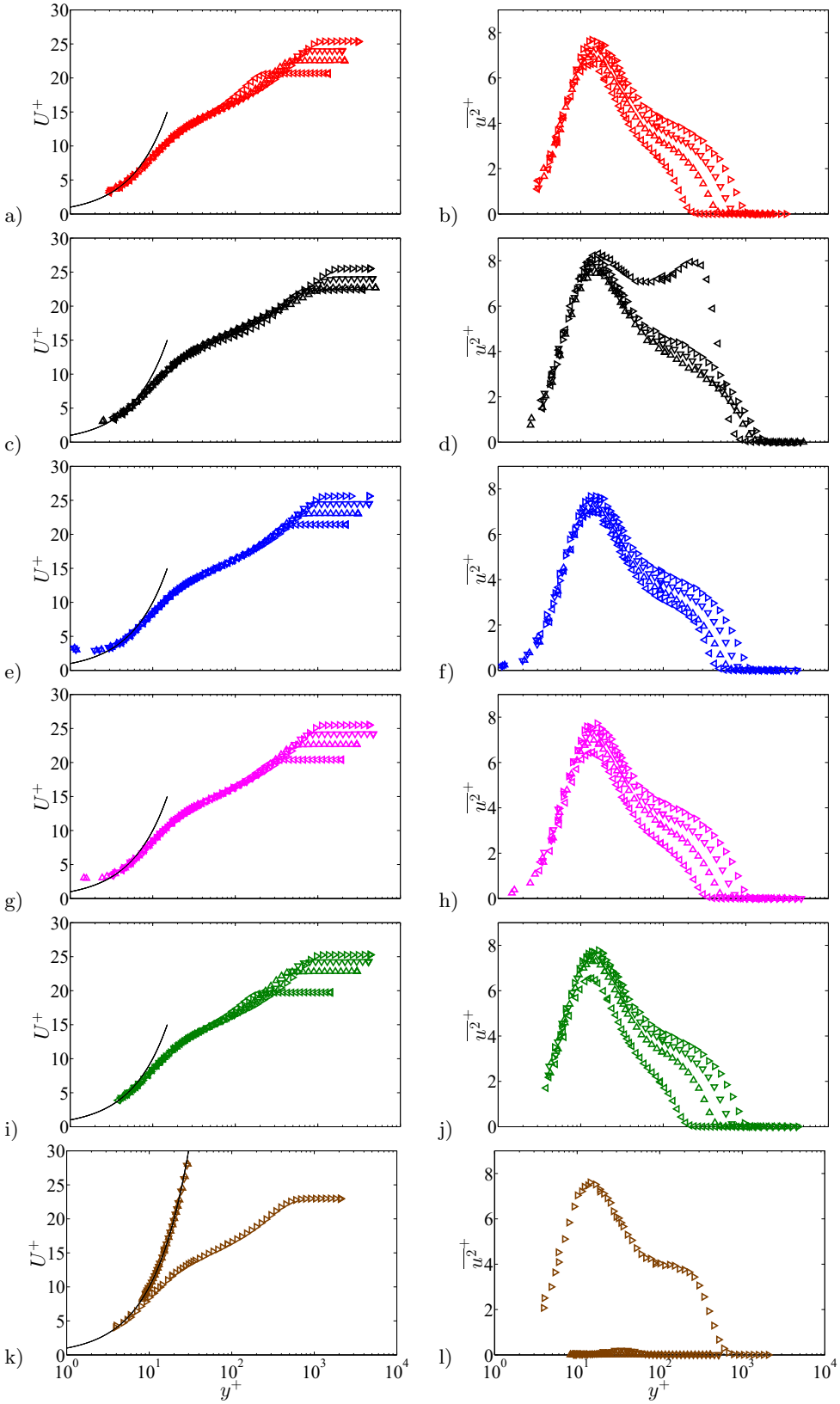

FIGURE 3. Evolution of inner-scaled mean streamwise velocity (left panels) and variance (right panels) profiles at ($\triangleleft$) $x = 0.24$ m, ($\triangle$) $x = 0.6$ m, ($\triangledown$) $x = 1.1$ m and ($\triangleright$) $x = 1.8$ m. Colors correspond to the various tripping configurations described in Table 1, while the solid lines depicts the linear profile $U^+ = y^+$.

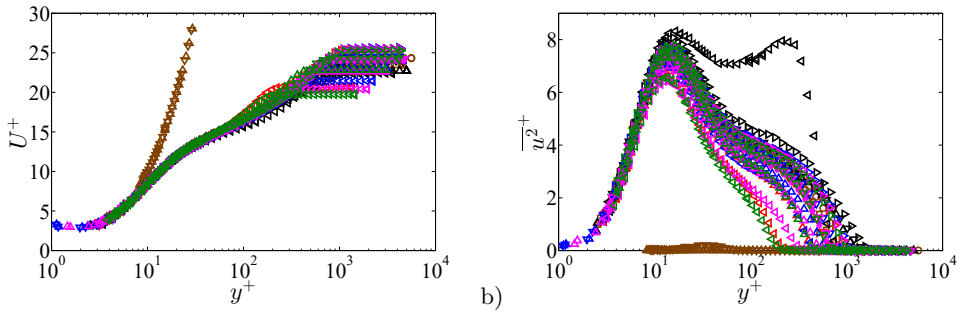

FIGURE 4. Inner-scaled a) mean streamwise velocity and b) variance profiles. Colors and symbols as in Figure 3, and additional measurement stations are represented by: (×) $x = 0.9$ m, (∗) $x = 0.95$ m, (□) $x = 2.1$ m and (○) $x = 2.5$ m.

260, the boundary layer remains essentially laminar for $x < 1.8$ m, as apparent from the linear profile ($U^+ = y^+$) that extends far beyond the usual bound of $y^+ \lesssim 5$. The two optimal cases, ③ and ④ (subplots e) and g)), exhibit similar developments in the buffer and overlap regions, with similar increase in U_∞^+ at the same streamwise measurement stations, which indicates that the development of the outer region is adequate (note that the missing point in the freestream present in one of the profiles from Figure 3e) is due to the fact that the traverse file erroneously was missing this point). The weak tripping case ① (subplot a)) shows that the first profile, at $x = 0.24$ m, is slightly underdeveloped in comparison with the equivalent profile in the optimal tripping cases ③ and ④: although the U_∞^+ value is similar to that of case ④, the overlap region deviates from the higher Re profiles earlier (at $y^+ \simeq 100$) compared with the optimal cases. The case ⑤ (subplot i)) exhibits a similar behavior at $x = 0.24$, with an even lower value of the inner-scaled freestream velocity related to the late transition and consequently lower friction Reynolds number Re_τ. The profiles downstream of this station are, in cases ① and ⑤, in good agreement with the optimal configurations ③ and ④. With respect to the strong trip case ② (subplot c)), the first profile at $x = 0.24$ m shows a more prominent wake region than the optimal cases, whereas at this first station the overlap region from case ② is beneath the optimal ones. These effects become attenuated downstream, where the profiles from the strong trip case progressively converge towards the optimal ones.

Regarding the streamwise variance profiles, the two optimal cases ③ and ④ also show an adequate development of the TBL, *i.e.* the inner and outer layers growth monotonically along the streamwise direction with only apparent differences in the first station. The mean flow deviation from the overlap region at around $y^+ \simeq 100$, observed at the first station of case ①, is also observed in the variance profile; at this location the variance decays faster than in the optimal case ④. Case ⑤ also shows fluctuation amplitudes below the optimal cases in the outer region, but, interestingly, cases ① and ⑤ progressively converge towards the variance profiles of the optimal cases, suggesting adequately that they recover from the weak tripping. With respect to case ⑥, the first profiles up to $x \simeq 1.8$ m also indicate the disturbance level is not sufficiently high to trigger transition to turbulence, as evinced from the fluctuation values close to zero throughout the whole boundary layer. The streamwise coordinate $x = 1.8$ m is the first one at which case ⑥ exhibits a near-wall fluctuation peak, although it clearly exhibits deviations with respect to the optimal cases. The first fluctuation profile from the strong tripping case ② is interesting in that respect since, in addition to an enhanced value of the near-wall peak, it also shows the emergence of an outer peak at $y^+ \simeq 250$, although the wall-normal

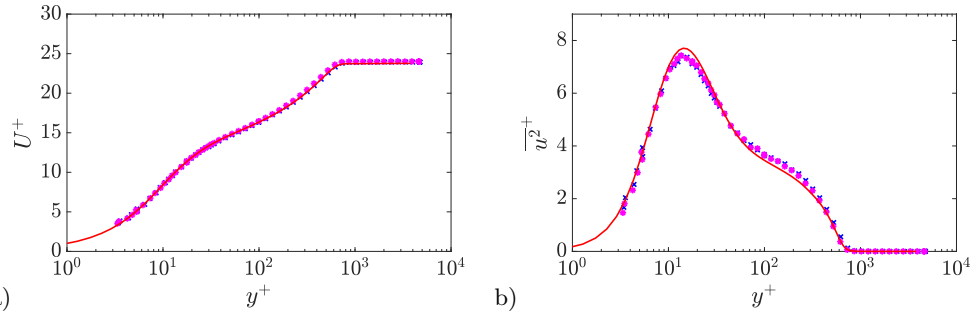

FIGURE 5. Inner-scaled a) mean streamwise velocity and b) variance profiles corresponding to the two optimal cases, *i.e.*, cases ③ and ④, at $Re_\theta \simeq 2,000$. Colors and symbols as in Figure 4, with the addition of the solid red line which represents the DNS results by Schlatter & Örlü (2010).

location is clearly beyond the inner layer as is the case for a canonical high Re ZPG TBL (Alfredsson *et al.* 2011). These effects in the outer region of the boundary layer, reminiscent of adverse-pressure-gradient TBLs (Monty *et al.* 2011*b*; Hosseini *et al.* 2016), were also observed by Tang *et al.* (2016) in their measurements of TBLs perturbed by a cylindrical roughness element. The outer peak in the fluctuations profiles progressively diminishes downstream of this location, as also observed by Tang *et al.* (2016), even if there is no complete convergence towards the optimal tripping profiles within the development lengths considered in the present study. These, effects, together with the ones observed in the mean flow, can be further examined in Figure 4, where all the mean and variance profiles for all stations shown in Table 3, including the ones not shown in Figure 3, are presented. Moreover, the two optimal cases, *i.e.*, cases ③ and ④, are compared at a matched Reynolds number of $Re_\theta \simeq 2,000$ with the DNS ZPG TBL data by Schlatter & Örlü (2010) in Figure 5. Note that the experimental profiles are obtained at slightly different streamwise locations, *i.e.*, at $x \simeq 0.90$ m in case ③ and at $x \simeq 0.95$ m in case ④, in order to obtain the matched value of Re_θ. This figure shows that both cases with optimal tripping are in excellent agreement with the numerical data, a conclusion that is observed both in the mean velocity and in the streamwise velocity fluctuation profiles. The results shown in Figure 5 are in agreement with the conclusions reported by Schlatter & Örlü (2012), in particular regarding the minimum value of $Re_\theta \simeq 2,000$ necessary to converge towards canonical ZPG TBL conditions.

3.2. *Comparison of TBLs at matched Reynolds number*

In order to emphasize the differences induced by the various tripping configurations under consideration, a comparison between cases at matched local momentum-thickness Reynolds numbers is shown. Figure 6 shows nominally matched $Re_\theta \approx 1,850$ cases of ①, ②, ④ and ⑥. For the mean streamwise velocity and variance, the profiles of cases ①, ④ and ⑥ are nearly identical. In the strong trip case ②, the profile exhibits a reduced wake region which shows that the influence of the initial condition, in form of a strong over-tripping, is still present. Regarding the pre-multiplied spectra of the streamwise velocity $f^+\Phi^+_{uu}$, which is shown in Figure 7, good agreement between all the cases, except ②, can be observed in the near-wall region where the inner peak is located at $y^+ \simeq 15$ and at a streamwise wavelength of $\lambda^+_x \simeq 1,000$ (when the period t^+ is converted into a wavelength through the local mean velocity as convection velocity). In the strong trip case ② the large-scale motions are clearly energized by the bar; since a strong outer peak is present in the spectra. Similar results of agreement between cases ①, ④ and ⑥ are observed

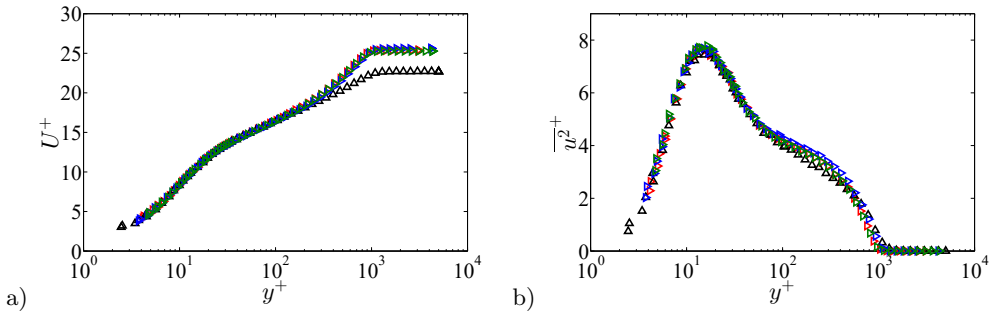

FIGURE 6. Inner-scaled a) mean streamwise velocity and b) velocity fluctuation profiles at matched $Re_\theta \approx 1,850$ for cases ①, ②, ④ and ⑥. Colors and symbols as in Figure 3, and streamwise locations reported in Table 1.

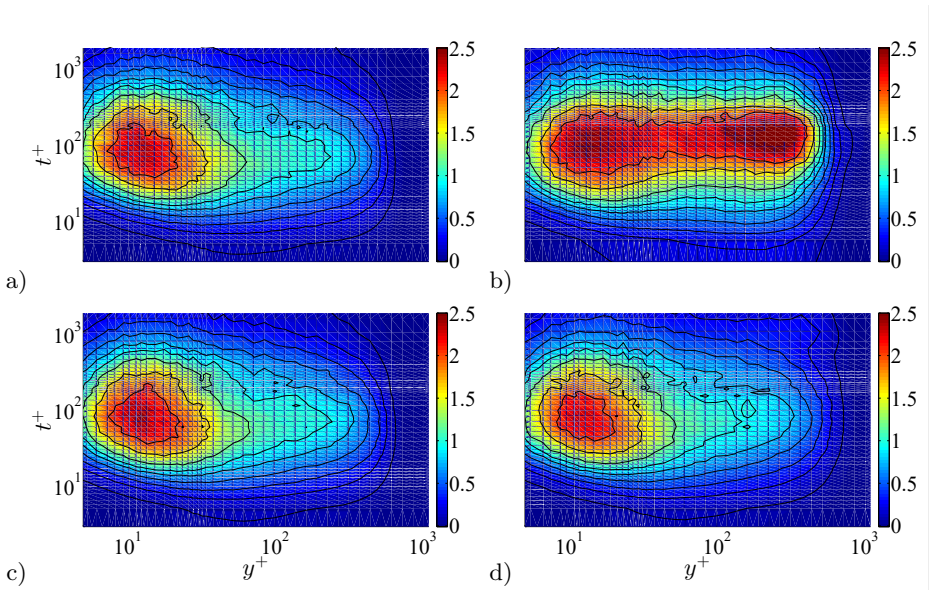

FIGURE 7. Inner-scaled streamwise premultiplied power spectral density of the streamwise velocity $f^+\Phi^+_{uu}$, at matched $Re_\theta \approx 1,850$. The following cases are shown: a) trip 1 at $x = 1.1$ m, b) trip 2 at $x = 0.24$ m, c) trip 4 at $x = 0.95$ m and d) trip 6 at $x = 2.1$ m. Contour levels are also highlighted at $f^+\Phi^+_{uu}$= 0.1, 0.25, 0.4, 0.575, 0.775, 0.95, 1.2, 1.6, 2 by black lines.

also for $Re_\theta > 3,000$. While the mean and variance profile for case ② for $Re_\theta > 3,000$ is nearly indistinguishable from the other cases, differences remain in the spectral energy distribution in the outer layer when compared to the other tripping cases.

4. Establishing criteria for identifying "well-behaved" profiles

In this section a study on the canonical behaviour of the profiles and their identification is presented. In §4.1 the criteria suggested by previous studies (Chauhan *et al.* 2009; Schlatter & Örlü 2012) are described, upon which a new method to identify well-behaved TBLs based on the diagnostic plot (Alfredsson *et al.* 2011) is proposed in §4.2, and is then finally applied in §4.3 to already existing DNS datasets combined with the criteria

outlined in §4.1 to identify, with minimal ambiguity, which profiles can be considered as canonical, and to validate the method.

4.1. *Existing criteria*

In order to discern which profiles can be considered as canonical, the evolution of the shape factor H, the skin-friction coefficient C_f, and the wake parameter Π, are considered as references. According to Chauhan *et al.* (2009), the wake parameter and the shape factor can be used as diagnostic quantities to assess whether a particular TBL can be considered to be canonical, since they have a high sensitivity to different boundary and inflow conditions. These quantities provide, in particular, an estimation of the degree of distortion in the outer part of the TBL, and require a long recovery distance to become independent of upstream disturbances (see also Schlatter & Örlü 2012). In this study, the reference curve chosen to characterise the shape factor is the one proposed by Monkewitz *et al.* (2007), which is obtained from asymptotic arguments, based on a vast number of experimental profiles covering a wide range of Reynolds numbers: $450 < Re_\theta < 125,000$. The equation proposed by Monkewitz *et al.* (2007) relates to H and Re_θ as follows:

$$H = 1 + \frac{\kappa I_{WW}}{\ln(Re_\theta)} + \frac{\kappa^2 I_{WW}(I_{WW} - C)}{\ln^2(Re_\theta)} + \frac{\kappa^2 I_{WW}\left(\kappa I_{WW}^2 - I_{WW} - 2\kappa I_{WW} C + \kappa C^2\right)}{\ln^3(Re_\theta)}, \tag{4.1}$$

with $\kappa = 0.384$, $I_{WW} = 7.11$ and $C = 3.3$. Regarding the evolution of the skin-friction coefficient C_f, the following Coles–Fernholz relation is considered:

$$C_f = 2\left[\frac{1}{\kappa}\ln\left(Re_\theta\right) + C'\right]^{-2}, \tag{4.2}$$

where the value of the von Kármán coefficient κ is also 0.384 and the constant C' takes the value 4.127. This choice of constants is due to Nagib *et al.* (2007), who established them based on a comprehensive analysis of experimental databases. Finally, the baseline streamwise-evolution of the wake parameter Π is obtained following the methodology proposed by Chauhan *et al.* (2009), based on the integration of the composite profile.

4.2. *Diagnostic-plot criterion*

The previous criteria rely on the computation of integral quantities, which often requires previous knowledge of other variables such as an accurate determination of the absolute wall position y and the friction velocity u_τ. These parameters are typically highly sensitive to experimental errors (Örlü *et al.* 2010). Moreover, the Reynolds-number evolution of other reference quantities such as H or Π can be defined in terms of several empirical curves. Furthermore, the application of the criteria described in §4.1 requires also an extensive experimental campaign (in terms of skin-friction and detailed mean velocity profile measurements), as well as intensive data processing, to identify whether and from which streamwise location on the TBL can be considered as well-behaved. For these reasons, here we propose an alternative method based on the so-called diagnostic-plot scaling introduced by Alfredsson *et al.* (2011). In this scaling, the root mean square of the streamwise velocity fluctuation u' is plotted against the mean velocity U, both normalised by the free-stream velocity U_∞. This plot has been shown to scale canonical ZPG TBL data over a wide range of Re throughout the logarithmic and outer region of ZPG TBLs (Alfredsson *et al.* 2012; Örlü *et al.* 2016). The diagnostic-plot was also found to scale pressure-gradient turbulent boundary layers (Drózdz *et al.* 2015) and thereby provide a robust method to determine the boundary layer thickness and the edge velocity

Case	Re_θ range	Color code
Schlatter & Örlü (2010)	600 – 4,300	Red
Eitel-Amor *et al.* (2014)	1,200 – 8,300	Brown
Jiménez *et al.* (2010)	1,100 – 2,000	Black
Sillero *et al.* (2013)	4,000 – 6,500	Blue
Wu *et al.* (2014)	650 – 3,100	Magenta
Khujadze & Oberlack (2004)	400 – 2,600	Green

TABLE 4. Summary of numerical databases under consideration in the present study, together with Re_θ ranges and color code.

in these flows (Vinuesa *et al.* 2016*a*), as well as scale rough-wall boundary layers (Castro *et al.* 2013) as well as a variety of wall-bounded and free-shear flows (Castro 2015). One of the greatest advantages of this scaling is the fact that according to Alfredsson *et al.* (2011), the data of canonical ZPG TBL collapse in the outer region, especially in the range $0.7 \leqslant U/U_\infty \leqslant 0.9$ (the lower limit further decreases with increasing Re, see Örlü *et al.* 2016), following a linear relation,

$$\frac{u'}{U} = \alpha - \beta \frac{U}{U_\infty}, \tag{4.3}$$

where α and β are fitting parameters. This means that the profiles that follow equation (4.3) in the outer region give "a good indication whether the boundary layer is in a natural state" (Alfredsson & Örlü 2010); although this was suggested in the first work on the diagnostic plot, it has not been systematically investigated with the focus on tripping and inflow effects as in the present work. The effect of Re_θ in the value of the parameters α and β is analysed in the following and is used to assess whether a boundary layer is considered well-beheaved or not. Note that the only data required to use this method are U and u' in the outer region, and U_∞. These measurements can be obtained easily at numerous stations from a simple hot-wire scan, without the need of any additional measurement such as y, u_τ, etc. Furthermore, measurements of turbulence quantities in the outer region are generally not subjective to spatial or temporal resolution issues. Therefore, this approach could be suitable to assess the development of turbulent boundary layers in a robust and efficient manner.

4.3. *Validation of the diagnostic plot method with numerical data*

In order to evaluate the ability of the method described in §4.2 to assess the convergence towards a canonical state of TBLs, here the method is applied to a number of ZPG TBL DNS datasets, namely the ones by Schlatter & Örlü (2010), Jiménez *et al.* (2010), Sillero *et al.* (2013), Wu *et al.* (2014) and Khujadze & Oberlack (2004), and to the well-resolved large-eddy simulation (LES) database by Eitel-Amor *et al.* (2014). Note that the particular Re_θ ranges of the various databases can be found in Table 4. The values of the free-stream velocity U_∞, the 99% boundary-layer thickness δ_{99} as well as other boundary-layer parameters have been recomputed following the procedure as outlined for the tripping experiments. In Figure 8 the numerical data are plotted in the diagnostic-plot form: subplot a) reports the profiles at all stations, while subplot b) reports only the profiles which fit to the diagnostic-plot outer scaling. In order to identify which profiles follow the diagnostic plot, only the profiles complying with both the H and C_f criteria to

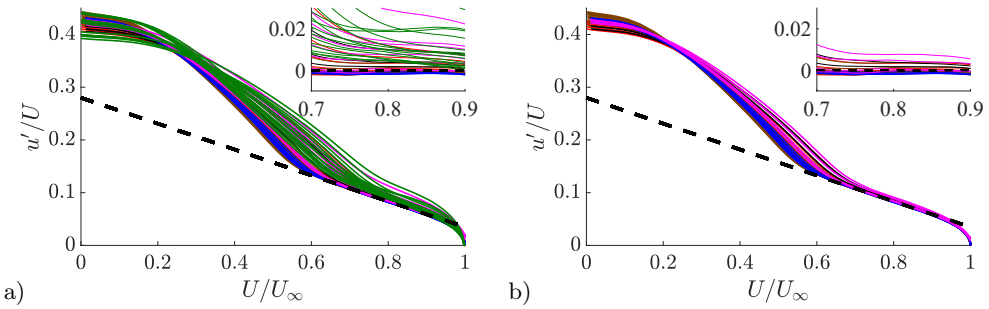

FIGURE 8. Diagnostic plot for a) all the numerical datasets and b) the numerical datasets that are considered well-behaved. Colors correspond to the cases summarized in Table 4. Dashed line represents equation (4.3) with $\alpha = 0.280$ and $\beta = 0.245$. Insets depict the difference between the data and equation (4.3) with the aforementioned constants.

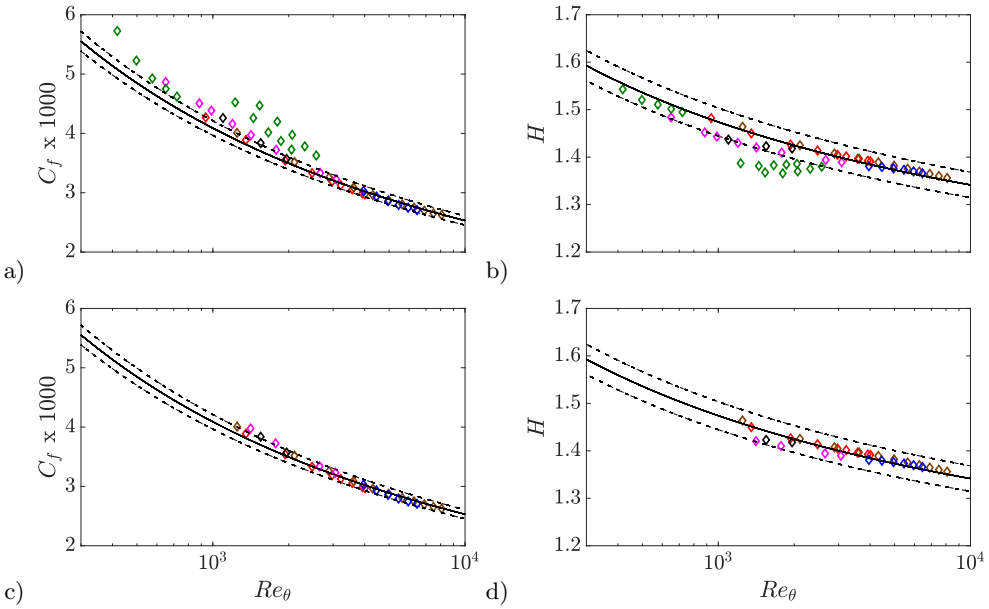

FIGURE 9. Skin-friction coefficient evolution with Re_θ for a) all the numerical datasets and c) the numerical profiles that follow the diagnostic-plot scaling given by equation (4.3), where the solid line is the reference given by equation (4.2) and ±3% deviation is represented by the dashed lines. Reynolds-number evolution of the shape factor H is given for b) all the numerical cases and d) the numerical profiles that follow (4.3), where the solid line shows the reference trend given by equation (4.1) and the dashed lines show ±2% deviation. Colors correspond to the cases summarized in Table 4.

within ±2% and 3% tolerance, respectively, have been considered, and fitting curves for α and β as function of Re_θ have been computed with the remaining data points. Then only the profiles with α, β and β/α complying with the fitting relations to within ±5%, ±5%, and ±2% tolerance, respectively, have been considered to properly fit the diagnostic plot (cf. 4.4). On the other hand, the H and C_f evolutions corresponding to all the numerical datasets are shown in Figure 9, together with the reference curves given by equations (4.1) and (4.2), respectively, as described in §4.1. It is interesting to note that the profiles that satisfy the diagnostic-plot criterion, *i.e.*, the ones shown in Figure 8b), are identical

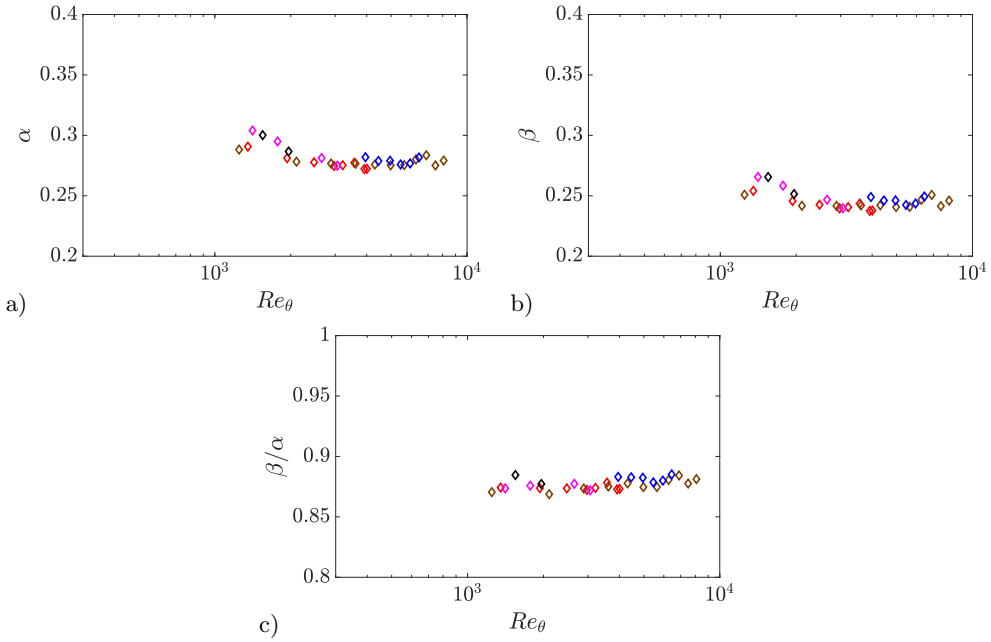

FIGURE 10. Evolution of the diagnostic-fit coefficients a) α and b) β, as well as the ratio c) β/α, with Re_θ. These coefficients are obtained from fits to equation (4.3), from the numerical databases described in Table 4, where the color code is also given.

to the ones that follow the reference H and C_f curves within $\pm 2\%$ and 3% tolerances, respectively, as shown in Figure 9. In accordance with previous studies (Schlatter & Örlü 2010, 2012), the diagnostic plot indicates, that all of the profiles from Khujadze & Oberlack (2004) exhibit non-canonical behaviour. The general agreement between the results from the inspection of the diagnostic plot and the criteria by Chauhan *et al.* (2009) is an argument in favour for the diagnostic-plot criterion described in §4.2 as a robust tool to assess whether a particular boundary layer exhibits canonical ZPG TBL conditions. In fact, the diagnostic plot can be used not only to discern well-behaved profiles, but also to recognize if a profile is fully-developed. From the insets of Figure 8, it can be observed that with increasing Re_θ the profiles tend to collapse. This fact can be better understood when the coefficients α and β of equation (4.3) are plotted as a function of Re_θ, as done in Figure 10. Note that these coefficients, obtained through fitting each individual profile to equation (4.3), exhibit an asymptotic behavior with Re, *i.e.*, α and β converge towards values around 0.280 and 0.245, respectively, for $Re_\theta > 2,000$. This observation is in accordance with the results by Schlatter & Örlü (2012), who established $Re_\theta \simeq 2,000$ as a threshold beyond which canonical features are exhibited by the ZPG TBL profiles, for cases in which transition was initiated at $Re_\theta < 300$. Moreover, Sillero *et al.* (2013) also claimed that the profiles with $Re_\theta < 2,000$ could not be considered fully developed. Interestingly, Figure 10 also shows that the ratio β/α shows an approximately constant value of around 0.876 for $Re_\theta > 1000$, which is the ratio of the asymptotic values of the two coefficients; note that values are rounded to two decimal places.

4.4. *Determination of the canonical boundary layer from experimental data*

After showing the ability of the diagnostic-plot method described in §4.2 to discern which numerical profiles exhibited canonical ZPG TBL conditions, we apply the same methodology to the experimental measurements to assess whether its results are in agreement

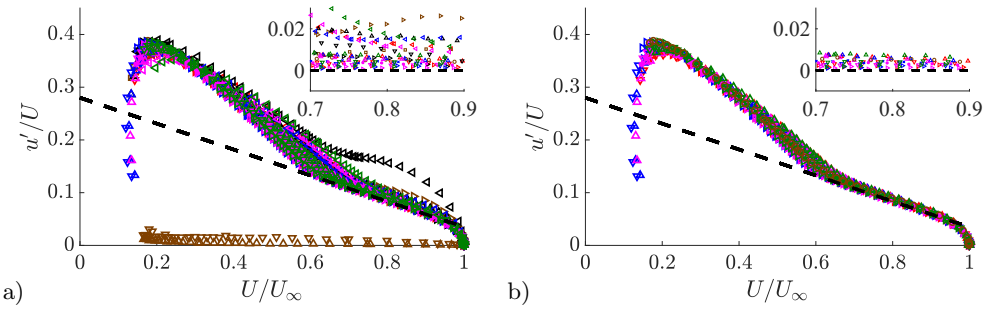

FIGURE 11. Diagnostic plot for a) all the experimental profiles and b) the experimental profiles that follow the diagnostic-plot scaling given by equation (4.3). Colors correspond to the cases summarized in Table 1. Dashed line represents equation (4.3) with $\alpha = 0.280$ and $\beta = 0.245$. Insets depict the difference between the data and equation (4.3) with the aforementioned constants.

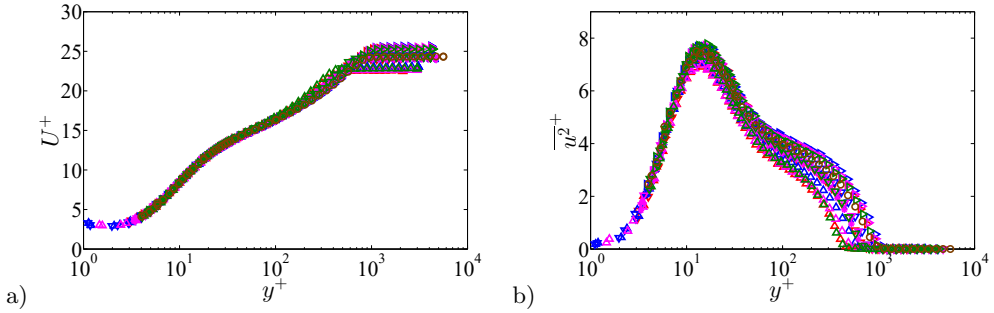

FIGURE 12. Inner-scaled a) mean streamwise velocity and b) variance profiles. Same data as in Figure 4, with the difference that profiles not passing the diagnostic-plot criteria are omitted.

with the other criteria described in §4.1. In Figure 11 all the experimental profiles summarized in Table 1 are presented in the diagnostic-plot form: subplot a) reports all cases, while subplot b) only reports the cases that follow the diagnostic scaling. Plotting now the profiles that remain in Figure 11b) in classical inner-scaling for the mean and variance, Figure 4 reduces to Figure 12, which exhibits the expected clear Reynolds-number trends in the wake profile for the mean velocity profile as well as the increase of the near-wall peak in the variance profile and the monotonic increase of the turbulence level in the outer layer.

Figure 13 depicts the Reynolds-number evolution of both C_f and H, and it is interesting to observe that, as in the numerical databases, the experimental profiles that follow the diagnostic-plot scaling are the ones consistent with the reference curves for both skin-friction coefficient and shape factor, as described in §4.1. All profiles which do not follow the diagnostic-plot criterion either fail according to the C_f or the H based criteria. For example, it can be observed that the cases which fulfil the H criterion (such as the lowest Re profile from the strong over-tripping case ②) but not the C_f criterion are clearly discarded by the diagnostic-plot approach. Therefore, the proposed methodology can also be used in experimental databases to assess the degree of convergence towards canonical conditions of a particular TBL configuration. Further support for this statement is given in Figure 14, where the coefficients from the diagnostic-plot equation (4.3) are calculated and shown as a function of Re_θ. Also in this case the profiles with $Re_\theta > 2,000$ exhibit

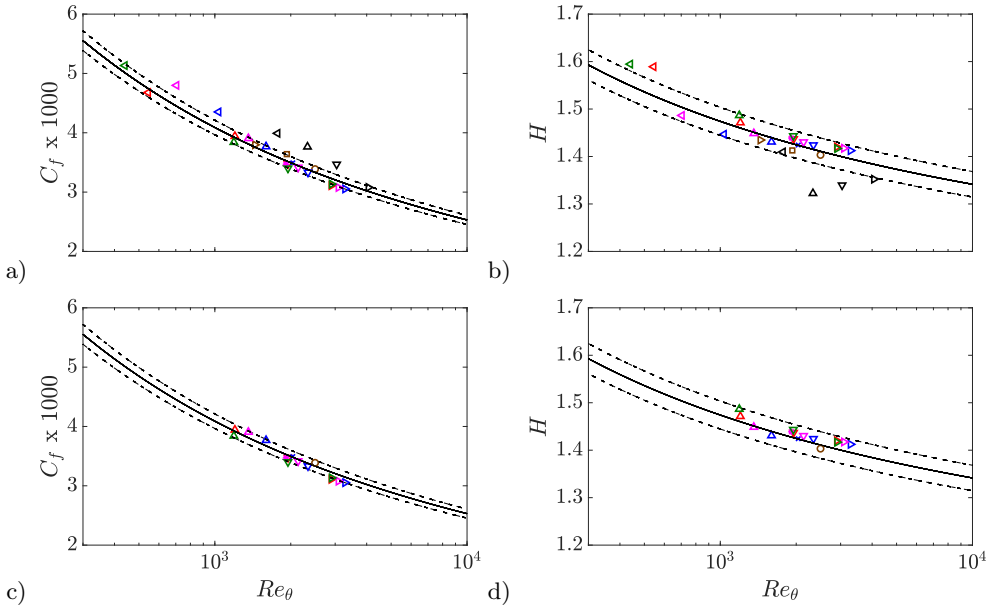

FIGURE 13. Skin-friction coefficient evolution with Re_θ for a) all the experimental profiles and c) the experimental profiles that follow the diagnostic-plot scaling given by equation (4.3), where the solid line is the reference given by equation (4.2) and ±3% tolerances are represented by the dashed lines. Reynolds-number evolution of the shape factor H is given for b) all the experimental cases and d) the experimental profiles that follow (4.3), where the solid line shows the reference trend given by equation (4.1) and the dashed lines show ±2% deviation. Colors correspond to the cases summarized in Table 3.

coefficients which asymptote to $\alpha \simeq 0.280$ and $\beta \simeq 0.245$. Interestingly, also in the experimental profiles the ratio β/α exhibits an approximately constant value of around 0.876 throughout the whole Reynolds-number range, as in the numerical databases shown in §4.3.

The evolution of the α and β coefficients is extended to higher Reynolds numbers by including in the analysis the experimental datasets by Bailey *et al.* (2013), Örlü & Schlatter (2013) and Vincenti *et al.* (2013) (except its highest Re data due to scatter and limited number of data points in the region in which α and β is determined). Note that in the extended database the maximum Re_θ is around 40,000. Following the same approach as in Figure 14, the diagnostic-plot coefficients are calculated for all the datasets from Tables 3 and 4, and for the three additional high-Re experimental datasets. In Figure 15 the Reynolds-number evolution of the coefficients α and β, together with the one of the ratio β/α, are shown for all the cases under consideration. The left panels show the cases where the particular profile follows the diagnostic-plot scaling, and the right panels the cases where the profiles do not follow it. It is interesting to note that all the high-Re datasets exhibit asymptotic values of α, β and β/α, which are consistent with the conclusions drawn from the previous, lower-Re datasets. Excluding the profiles on the right panels, which do not follow the diagnostic scaling, it is possible to establish the following empirical fits defining the Re_θ evolutions of α and β:

$$\alpha = 0.280 + 20/Re_\theta, \tag{4.4}$$

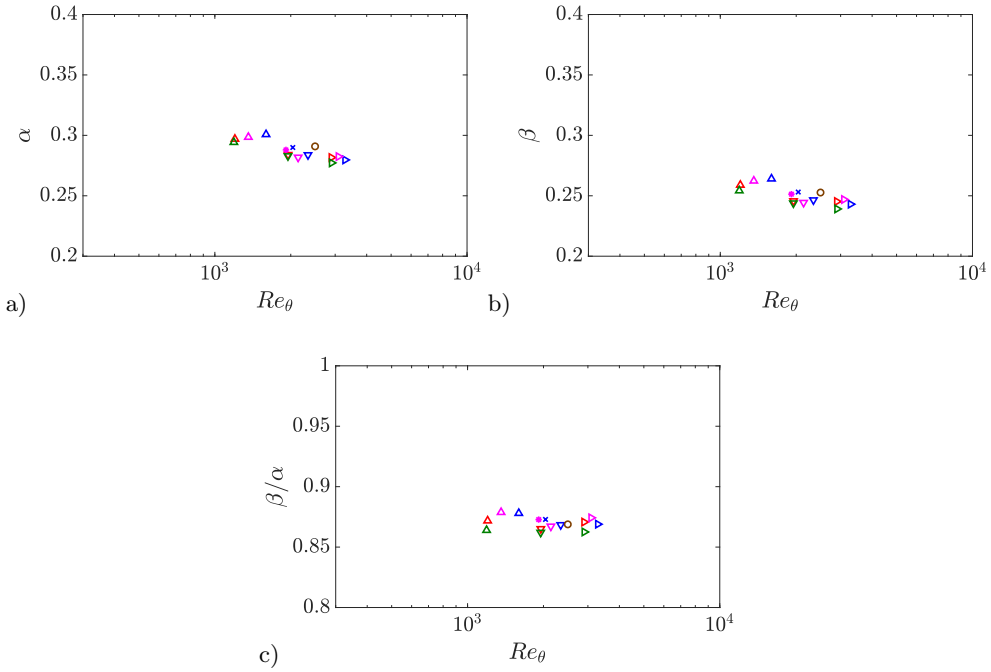

FIGURE 14. Evolution of the diagnostic-plot coefficients a) α and b) β, as well as c) the ratio β/α, with Re_θ. These coefficients are obtained from fits to equation (4.3), from the experimental databases described in Table 3, where the color code is also given.

$$\beta = 0.245 + 17.5/Re_\theta. \tag{4.5}$$

These curves are also shown in Figure 15, where it can be observed that all the profiles in subplots a) and c) follow these trends within $\pm 5\%$. Moreover, Figure 15e) shows that the ratio β/α is approximately constant and equal to $\simeq 0.876$ for the whole Re-range in all the profiles following the diagnostic scaling. All the profiles in this subplot exhibit deviations in β/α within $\pm 2\%$ with respect to 0.876, which is an interesting conclusion regarding the applicability of the diagnostic-plot method for assessment of well-behaved profiles at low Re. With respect to the profiles shown in the right panels of Figure 15, it is clear that α and β do not follow the relations given by equations (4.4) and (4.5), and the ratio β/α deviates from 0.876. Interestingly, the cases that do not satisfy the diagnostic-plot scaling are not consistent with the C_f and H equations (4.2) and (4.1) presented above either, which shows additional support for the use of the methodology based on the diagnostic-plot method, and additionally highlights the consistency of the various approaches to characterize the TBL development. In fact, there are few cases in Figure 15 (right) in which the trend of a particular coefficient is followed, but only the profiles for which the evolution of the two coefficients is consistent with the empirical fits also satisfy both the skin-friction and shape-factor criteria.

The discussion above shows that the diagnostic-plot criterion, which only requires measurements of the streamwise mean velocity and turbulence intensity is consistent with other methods such as the skin-friction coefficient curve, which requires accurate measurements of the wall-shear stress, or the shape-factor curve for which full velocity profile measurements are required. Note that it may not be straightforward to determine

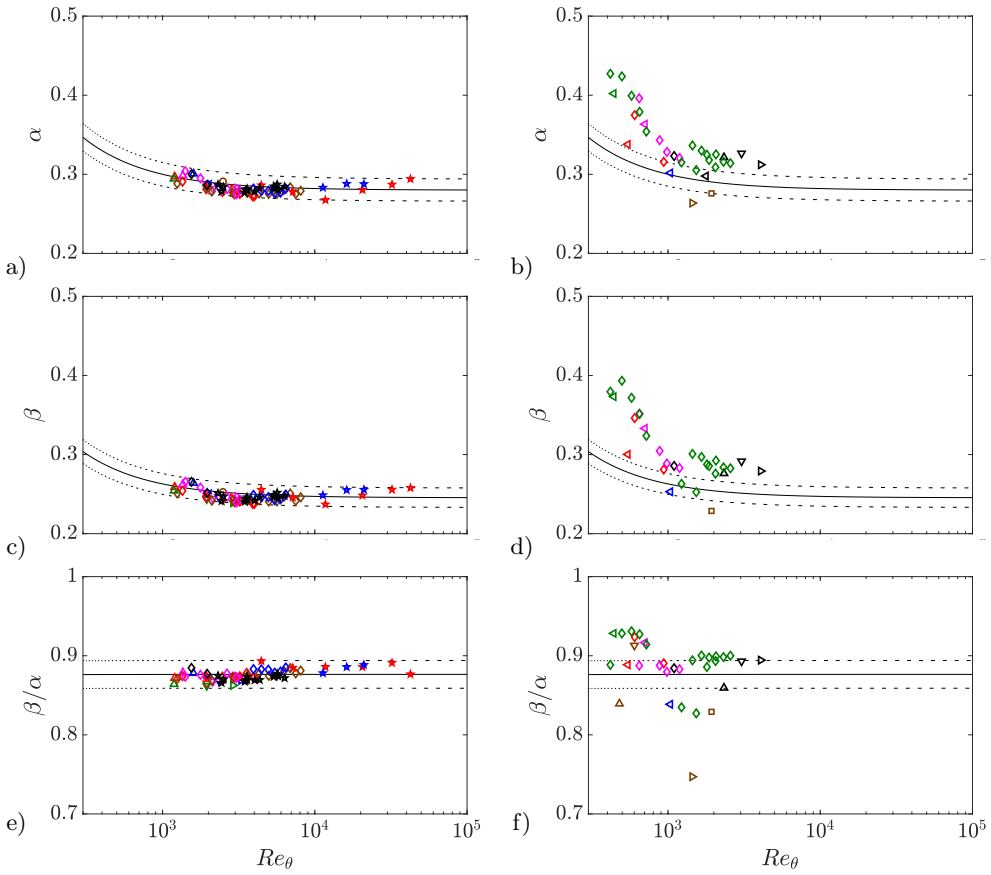

FIGURE 15. Evolution with Re_θ of diagnostic-plot coefficients a–b) α and c–d) β from equation (4.3), as well as e–f) their ratio β/α, for all experimental and numerical (indicated by $\diamond$) datasets summarised in Tables 3 and 4, respectively. Additional, high-Re experimental datasets are represented by the following symbols: (blue star) Bailey *et al.* (2013), (black star) Örlü & Schlatter (2013) and (red star) Vincenti *et al.* (2013). Left panels show the profiles that follow the diagnostic-plot scaling (4.3), whereas the data shown in the right panels do not follow it. Black solid lines represent the empirical fits for α and β given by equations (4.4) and (4.5), respectively, as well as the ratio $\beta/\alpha \simeq 0.876$. Dashed lines represent $\pm 5\%$ deviation with respect to equations (4.4) and (4.5), and $\pm 2\%$ deviation with respect to $\beta/\alpha \simeq 0.876$.

the location of the wall directly and/or accurately in hot-wire measurements, especially at high Reynolds numbers where the viscous length scale becomes progressively smaller (Örlü *et al.* 2010; Vinuesa *et al.* 2016*b*). For this reason, in the present work we propose a methodology based on the diagnostic plot given by equation (4.3), and the evolution with Re of its parameters. In order to discern if a ZPG TBL is well-behaved, it is only necessary to analyze the mean velocity and turbulence intensity profiles in the range $0.7 < U/U_\infty < 0.9$, where a linear fit can be used to obtain the values of α, β and β/α. These parameters can be compared with equations (4.4) and (4.5) for α and β, and with the value 0.876 for the ratio β/α. As shown in Figure 15, if the values of α and β lie within $\pm 5\%$ of the values predicted by equations (4.4) and (4.5), and if β/α is within $\pm 2\%$ of 0.876, the ZPG TBL profile can be considered to be well-behaved. Note that since the trends discussed above are valid for $Re_\theta > 1,000$, in cases where Re_θ is unknown the procedure to ensure convergence towards a canonical state is to

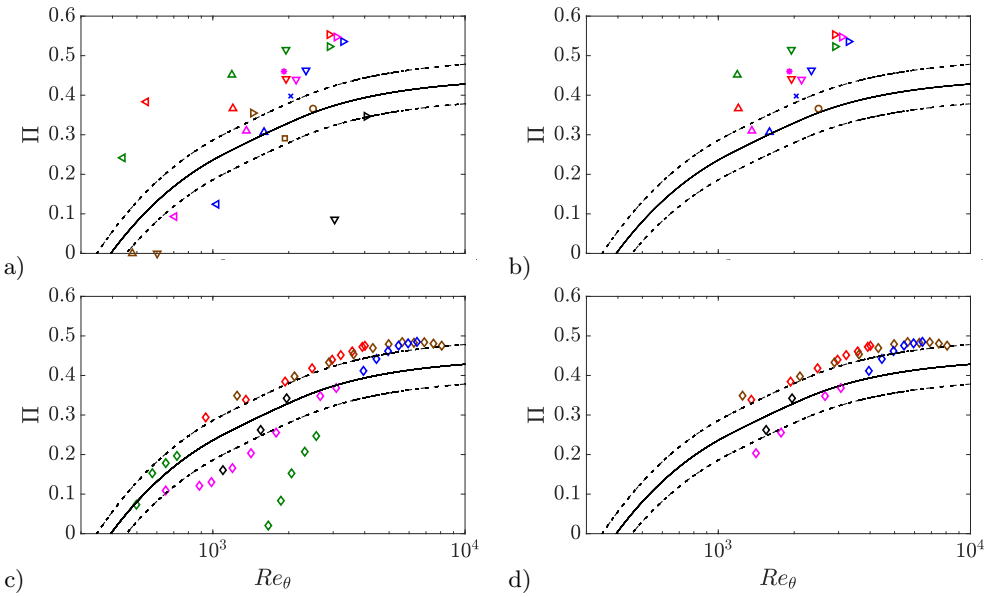

FIGURE 16. Reynolds-number evolution of the wake parameter Π from a) all the experimental profiles summarized in Table 3, b) the profiles that follow the diagnostic-plot scaling (4.3), c) all the numerical datasets and d) the numerical datasets that follow the diagnostic-plot scaling given by equation (4.3) . Solid line is obtained through integration of the composite profile as in Chauhan *et al.* (2009), and dashed lines represent ±0.05 deviation.

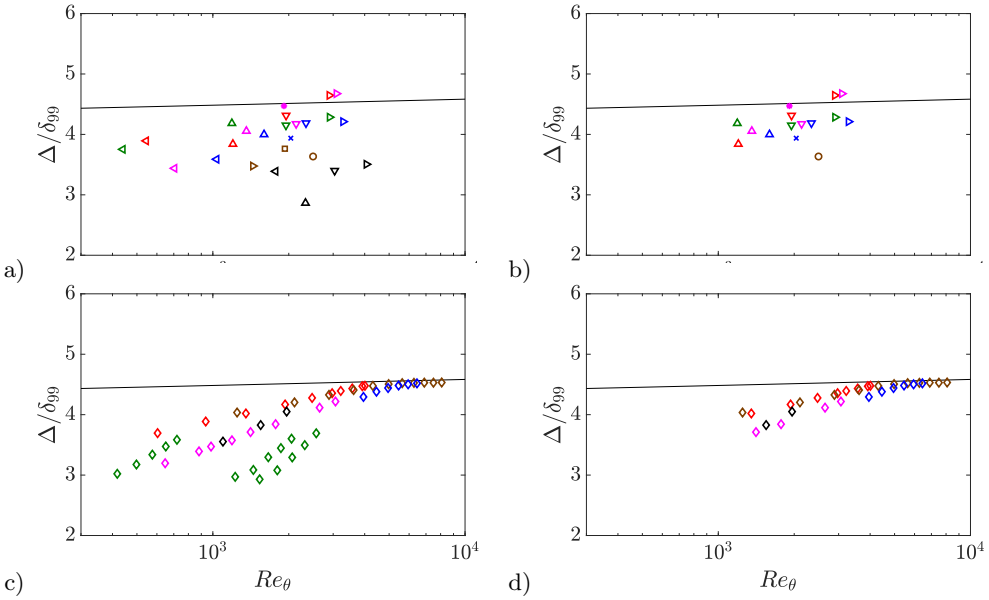

FIGURE 17. Reynolds-number evolution of Δ/δ_{99} from a) all the experimental profiles summarized in Table 3, b) the experimental profiles that follow the diagnostic-plot scaling (4.3), c) all the numerical datasets and d) the numerical datasets that follow the diagnostic-plot scaling given by equation (4.3). Solid line shows the reference trend given by Nagib *et al.* (2007).

obtain α, β and β/α at several streamwise locations and study the convergence of these values towards the predicted asymptotic values, *i.e.*, $\alpha \simeq 0.280$ and $\beta \simeq 0.245$. The use of the diagnostic-plot methodology proposed here shows the advantage with respect to the shape-factor method of relying only on the scaling of mean velocity and turbulence intensity in the outer region of the TBL. Moreover, the method proposed by Chauhan *et al.* (2009) based on the wake parameter Π is also tested here, and compared with the outcome of the other methods discussed above. Note that the wake parameter is a very sensitive quantity, which requires accurate measurements of the inner-scaled mean velocity profile (including u_τ and y), relies on composite fits to calculate the value of Π and is directly dependent on the log-law constants/coefficients; an issue of ambiguity on its own for low-Re data sets. In Figure 16a) we show the evolution with Re of the wake parameter calculated from all the experimental profiles; note that the calculation of Π was performed based on the method proposed by Chauhan *et al.* (2009), and the reference Π evolution with Re_θ was determined through integration of the composite profile proposed in the same work. On the other hand, in Figure 16b) we show the Π curve from the profiles that satisfy the diagnostic-plot criterion (which also satisfy the skin-friction and shape-factor criteria as discussed above). As expected, the profiles that do not satisfy the diagnostic-plot method also deviate from the Π curve proposed by Chauhan *et al.* (2009), and do not exhibit any consistent trend with Reynolds number. Furthermore, the profiles that follow the diagnostic-plot method exhibit an increasing trend of Π with Re_θ, similar to the one shown by the curve from Chauhan *et al.* (2009), although they appear consistently shifted upwards by around $\simeq 0.1$. This shows that, although the wake parameter is also a good indicator of the state of the boundary layer, and in particular of its convergence towards canonical ZPG TBL conditions, it is very sensitive to a number of factors and experimental uncertainties, including details of the tripping mechanism and of the fit, and therefore shows more difficulties when used to assess in detail the conditions of the TBL. It should also be noted that the Π values given here (in accordance with Chauhan *et al.* 2009) are obtained with fixed log-law parameters, which explains that very low and even negative values can be obtained; cf. values in table 3. To underline this point, subplots c) and d) depict the same plots for the DNS data discussed in §4.3 which besides removing data points with low Re-effects also indicates that most of the data sets lie actually above, but parallel to, the curve from Chauhan *et al.* (2009) in accordance with the experimental data shown in subplots a) and b).

In addition to the Π criterion, the evolution of the Rotta-Clauser length scale $\Delta = U_\infty \delta^*/u_\tau$ normalized with the boundary-layer thickness defined here as δ_{99} is also studied. According to the work by Nagib *et al.* (2007), the ratio Δ/δ_{99} can also be used to assess the evolution of a TBL towards a well-behaved state independent of the inflow conditions. In Figures 17a) and c) we show the Reynolds-number evolution of Δ/δ_{99} for all the experimental and numerical cases under consideration, where it can be observed that a number of profiles exhibit Δ/δ_{99} values below the trend reported by Nagib *et al.* (2007). This is associated with profiles which have not reached a state independent of the inflow conditions, and therefore subjected to non-equilibrium effects. In Figures 17b) and d) we only show the experimental and numerical profiles that follow the diagnostic-plot scaling given by equation (4.3). It can be observed that the profiles above $Re_\theta \simeq 2,000$ are in good agreement with the curve developed by Nagib *et al.* (2007), whereas the ones below this Reynolds number follow a similar trend, with slightly lower values. Also note that the higher-Re profiles exhibit a value of Δ/δ_{99} approximately equal to 4.5, which is consistent with the observations by Nagib *et al.* (2007). Therefore, the method proposed in the present work based on the diagnostic plot is in reasonably good agreement with

the approach to assess well-behaved profiles based on Δ/δ_{99}, proposed by Nagib *et al.* (2007).

4.5. *Diagnostic-plot methodology as a design tool*

The previous sections have shown that the proposed diagnostic-plot methodology is a reliable technique to evaluate the development of ZPG TBLs towards canonical conditions, which only requires measurements of the streamwise mean and turbulence intensity in the outer region of the boundary layer. Since neither the skin-friction coefficient, shape factor or wake parameter, nor full velocity profile measurements are required, the idea to assess the streamwise development with a scan through the outer part of the TBL arose. More specifically, here we demonstrate that by placing a hot-wire probe within the outer part of the boundary layer and traversing it downstream by keeping it within the outer region of the TBL, the streamwise location from where on the TBL can be considered genuine and well-behaved is estimated to be when the measured turbulence intensity falls on relation (4.3) with the established constants. Figure 18 shows the results from a streamwise traverse while keeping (through an iterative procedure) the probe within the velocity range $0.7 < U/U_\infty < 0.9$ through the outer part of a ZPG TBL corresponding to the tripping configuration ⑥. As apparent from the color-coded measurement points, indicating the streamwise distance from the leading edge (from lighter to darker symbols with increasing streamwise distance), the boundary layer is first laminar and then undergoes transition to turbulence with the associated overshoot in turbulence intensity (in accordance with figures 3k–l) somewhere between the 1.1 m and 1.8 m stations. Since the measurement points are taken with an equidistant streamwise spacing, it is apparent from the accumulation of measurement points that the outer layer requires long development lengths to overcome the post-transitional stage and behave in accordance with the diagnostic scaling. It is interesting to note that the profiles in the post-transitional regime for $x \geqslant 1.8$ m actually agree very well with the empirical curves for the skin-friction coefficient, shape factor and wake parameter. According to the diagnostic plot, the first point that complies with the diagnostic scaling corresponds to x =1.90 m, which agrees sufficiently well with the results shown in figure 13. Note that albeit the exact location of the range $0.7 < U/U_\infty < 0.9$ is not known a priory, the traverse can still be taken in an automated way by iterating until the measured mean velocity is within the desired percentage of the free-stream velocity.

5. Summary and Conclusions

The impact of tripping devices on the development of zero-pressure-gradient turbulent boundary layers is assessed in the present study by means of hot-wire anemometry measurements. To that end, a total of six tripping configurations, including optimal set-ups and both under and over-tripping cases, are used. A total of 27 velocity profiles are measured over the Reynolds number range $440 < Re_\theta < 4,070$, and their evolutions from the various inflow conditions are compared at matched streamwise locations from the flat-plate leading edge, and also at matched Re_θ conditions. Our results show that the weak tripping cases lead to deviations in the logarithmic region of the inner-scaled mean flow (at around $y^+ \simeq 100$) with respect to the optimum tripping, whereas the over-tripping case leads to a more prominent wake. Regarding the effect in the streamwise variance profile, the weak trip cases also lead to small deviations with respect to the optimum tripping at around $y^+ \simeq 100$, where the fluctuation levels are lower. The strong tripping case leads to an enhanced inner peak as well as to the development of an outer peak in the variance profile. This effect was also observed in the experiments by Tang *et al.*

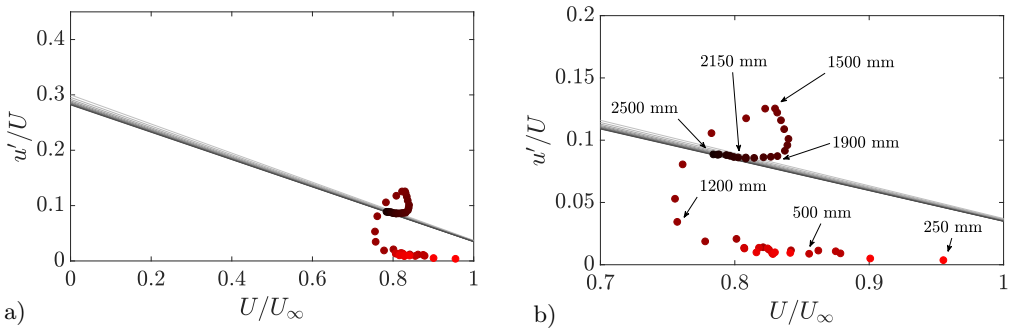

FIGURE 18. a) Diagnostic-plot methodology as a design tool demonstrated using the ZPG TBL with the tripping configuration ⑥, *i.e.* the weak, very late tripping. Solid lines correspond to equation (4.4)–(4.5) with $Re_\theta = 1,000$ (light grey) to 10,000 (dark grey) (10 logarithmically spaced cases). b) Zoom-in of a) with indicated streamwise locations of the measurement points taken with equidistanc streamwise spacings of $\Delta x = 50$ mm.

(2016), and suggests that the strong tripping energizes the large-scale motions in the outer part of the boundary layer, as in adverse-pressure-gradient TBLs (Monty *et al.* 2011*b*; Hosseini *et al.* 2016), and supported by spectral analysis.

Development of TBLs towards canonical conditions have from early days of turbulent-boundary-layer research (Coles 1968) been assessed based on the streamwise evolution of quantities such as the skin-friction coefficient C_f, the shape factor H and the wake parameter Π and this is still the common way in the literature (Chauhan *et al.* 2009; Marusic *et al.* 2015). Extensive analysis of a wide range of experimental databases has led to a number of empirical relations for these evolution of the three parameters, as discussed in §4.1, and convergence towards canonical conditions can be assessed with respect to such reference curves. It is important to note that accurate measurements of the friction velocity u_τ are necessary for an assessment based on C_f, and that an accurate location of the wall y is required to obtain the shape-factor curve. Furthermore, the wake parameter relies on measurements of the inner-scaled mean velocity profile and is a very sensitive parameter that requires the use of composite profiles in order to be calculated. In the present study we assess the possibility of using the diagnostic-plot method (Alfredsson *et al.* 2011). The advantage of this method is that it only relies on measurements of the streamwise mean velocity and turbulence intensity at arbitrary wall-normal distances, and therefore uncertainties from u_τ or y, among others, are eliminated with its use. The measurements conducted as part of this experimental campaign, as well as several numerical databases up to $Re_\theta = 8,300$, show that the diagnostic-plot method proposed here, while extremely simple in its application, provides results equivalent to the C_f and H curves when assessing the convergence of a TBL towards canonical conditions. It is important to note that the current diagnostic-plot approach is based on a limited Re-range, in which a completely developed overlap layer cannot be observed yet. However, the assessment of whether a particular profile can be considered canonical or not is consistent with the C_f and H correlations, obtained over wider Reynolds-number ranges. Moreover, none of these methods would guarantee convergence towards canonical conditions in the limit of infinite Reynolds number. In addition to this, analysis of the α and β coefficients from the diagnostic-plot curve (4.3) from the canonical profiles shows that they reach approximately constant values of $\alpha \simeq 0.280$ and $\beta \simeq 0.245$ for $Re_\theta > 2,000$. Although additional data at higher Reynolds numbers would be required to assess whether these are the asymptotic values of α and β, they allow to formulate a robust criterion to assess

the initial development of the boundary layer. In fact, this is in good agreement with the results by Schlatter & Örlü (2012), who established $Re_\theta \simeq 2,000$ as a threshold beyond which canonical features are exhibited by the ZPG TBL profiles, *i.e.*, below which low Re-effects need to be accounted for. Empirical relations for the evolution of α and β with Re_θ are provided in order to extend the diagnostic-plot criterion also to the low Re_θ range. The ratio β/α is practically independent of Re, once $Re_\theta > 1000$, and approximately equal to 0.876 for well-behaved profiles. Note that although the empirical relations have been additionally verified with high-Re datasets (up to $Re_\theta \simeq 40000$), the conclusions in the present work are based on low-Re data, as well as on streamwise mean and fluctuating velocity profiles.

The diagnostic-plot methodology proposed in the present study is therefore a reliable technique to evaluate the development of ZPG TBLs towards canonical conditions, which only requires measurements of the streamwise mean and turbulence intensity, in the outer region of the boundary layer. This is a great advantage in comparison to methods based on skin-friction coefficient, shape factor or wake parameter, which require more involved measurements of friction velocity, accurate wall position and use of composite profiles. The mentioned features of the diagnostic-plot methodology can be exploited to determine the streamwise location from where on the ZPG TBL is well-behaved, by simply traversing the measurement probe through a portion of the outer region until the measured turbulence intensity falls on top of the diagnostic scaling. Equivalently, the method is shown to provide a quick diagnostic tool to assess the quality of numerical data as well.

Acknowledgements

CSV acknowledges the financial support from Universidad Carlos III de Madrid within the program "Ayudas para la Movilidad del Programa Propio de Investigación". RÖ, RV and PS acknowledge the financial support from the Swedish Research Council (VR) and the Knut and Alice Wallenberg Foundation. CSV, SD and AI were partially supported by the COTURB project (Coherent Structures in Wall-bounded Turbulence), funded by the European Research Council (ERC), under grant ERC-2014.AdG-669505. AI, CSV and SD have been partially supported by grant DPI2016-79401-R of the Spanish Mineco.

REFERENCES

Alfredsson, P. H. & Örlü, R. 2010 The diagnostic plot — a litmus test for wall bounded turbulence data. *Eur. J. Mech. B/Fluids* **29**, 403–406.

Alfredsson, P. H., Örlü, R. & Segalini, A. 2012 A new formulation for the streamwise turbulence intensity distribution in wall-bounded turbulent flows. *Eur. J. Mech. B/Fluids* **36**, 167–175.

Alfredsson, P. H., Segalini, A. & Örlü, R. 2011 A new scaling for the streamwise turbulence intensity in wall-bounded turbulent flows and what it tells us about the "outer" peak. *Phys. Fluids* **23**, 041702.

Bailey, S. C. C., Hultmark, M., Monty, J. P., Alfredsson, P. H., Chong, M. S., Duncan, R. D., Fransson, J. H. M., Hutchins, N., Marusic, I., Mckeon, B. J., Nagib, H. M., Örlü, R., Segalini, A., Smits, A. J. & Vinuesa, R. 2013 Obtaining accurate mean velocity measurements in high reynolds number turbulent boundary layers using pitot tubes. *J. Fluid Mech.* **715**, 642–670.

Castillo, L. & Johansson, T. G. 2002 The effects of the upstream conditions on a low Reynolds number turbulent boundary layer with zero pressure gradient. *J. Turbul.* **3**, 1–19.

Castro, I. A. 2015 Turbulence intensity in wall-bounded and wall-free flows. *J. Fluid Mech.* **770**, 289–304.

Castro, I. A., Segalini, A. & Alfredsson, P. H. 2013 Outer-layer turbulence intensities in smooth- and rough-wall boundary layers. *J. Fluid Mech.* **727**, 119–131.

Chauhan, K. A., Monkewitz, P. A. & Nagib, H. M. 2009 Criteria for assessing experiments in zero pressure gradient boundary layers. *Fluid Dyn. Res.* **41**, 021404.

Coles, D. E. 1956 The law of the wake in the turbulent boundary layer. *J. Fluid Mech.* **1**, 191–226.

Coles, D. E. 1962 The turbulent boundary layer in a compressible fluid. *Rand. Rep. R-403-PR* .

Coles, D E 1968 The young person's guide to the data. *AFOSR-IFP-Stanford Conf. on Computation of turbulent boundary layers, D. E. Coles and E. A. Hirst (Eds.), pp. 1–45* .

Dróżdz, A, Elsner, W & Drobniak, S 2015 Scaling of streamwise Reynolds stress for turbulent boundary layers with pressure gradient. *Eur. J. Mech. B-Fluid* **49**, 137–145.

Eitel-Amor, G., Örlü, R. & Schlatter, P. 2014 Simulation and validation of a spatially evolving turbulent boundary layer up to $Re_\theta = 8300$. *Int. J. Heat Fluid Flow* **47**, 57–69.

Erm, L. P. & Joubert, P. N. 1991 Low-Reynolds-number turbulent boundary layers. *J. Fluid Mech.* **230**, 1–44.

Fernholz, H. H. & Finley, P. J. 1996 The incompressible zero-pressure-gradient turbulent boundary layer: An assessment of the data. *Prog. Aero. Sci.* **32**, 245–311.

Hosseini, S. M., Vinuesa, R., Schlatter, P., Hanifi, A. & Henningson, D. S. 2016 Direct numerical simulation of the flow around a wing section at moderate reynolds number. *Int. J. Heat Fluid Flow* **61**, 117–128.

Hultmark, M, Bailey, S. C. C. & Smits, A. J. 2010 Scaling of near-wall turbulence in pipe flow. *J. Fluid Mech.* **649**, 103–113.

Hutchins, N 2012 Caution: tripping hazards. *J. Fluid Mech.* **710**, 1–4.

Hutchins, N., Monty, J. P., Hultmark, M. & Smits, A. J. 2015 A direct measure of the frequency response of hot-wire anemometers: temporal resolution issues in wall-bounded turbulence. *Exp. Fluids* **56**, 18.

Hutchins, N., Nickels, T. B., Marusic, I. & Chong, M. S. 2009 Hot-wire spatial resolution issues in wall-bounded turbulence. *J. Fluid Mech.* **635**, 103–136.

Jiménez, J., Hoyas, S., Simens, M. P. & Mizuno, Y 2010 Turbulent boundary layers and channels at moderate Reynolds numbers. *J. Fluid Mech* **657**, 335–360.

Khujadze, G. & Oberlack, M. 2004 DNS and scaling laws from new symmetry groups of ZPG turbulent boundary layer flow. *Theor. Comput. Fluid Dyn.* **18**, 391–411.

Klebanoff, P. S. & Diehl, W. S. 1954 Some features of artificially thickened fully developed turbulent boundary layers with zero pressure gradient. *NACA Tech. Rep. 1110* .

Kozul, M., Chung, D. & Monty, J. P. 2016 Direct numerical simulation of the incompressible temporally developing turbulent boundary layer. *J. Fluid Mech.* **796**, 437–472.

Lee, J. H., Kwon, Y S, Monty, J. P. & Hutchins, N. 2014 Time-resolved piv measurement of a developing zero pressure gradient turbulent boundary layer. *In Proceedings of the 19th Australasian Fluid Mechanics Conference, 8th-11th December 2014 (ed. P. A. Brandner B. W. Pearce). Australasian Fluid Mechanics Society.* .

Lindgren, Björn & Johansson, A. V. 2002 Evaluation of the flow quality in the MTL windtunnel. *Tech. Rep., Royal Institute of Technology (KTH), Stockholm, Sweden* .

Lund, T., Wu, X. & Squires, K. 1998 Generation of turbulent inflow data for spatially-developing boundary layer simulations. *J. Comput. Phys.* **140**, 233–258.

Marusic, I., Chauhan, K. A., Kulandaivelu, V. & Hutchins, N. 2015 Evolution of zero-pressure-gradient boundary layers from different tripping conditions. *J. Fluid Mech.* **783**, 379–411.

Marusic, I., McKeon, B. J., Monkewitz, P. A., Nagib, H. M., Smits, A. J. & Sreenivasan, K. R. 2010 Wall-bounded turbulent flows at high Reynolds numbers: Recent advances and key issues. *Phys. Fluids* **22**, 065103.

Monkewitz, P. A., Chauhan, K. A. & Nagib, H. M. 2007 Self-consistent high-Reynolds-number asymptotics for zero-pressure-gradient turbulent boundary layers. *Phys. Fluids* **19**, 115101.

Monty, J. P., Harun, Z. & Marusic, I. 2011*a* A parametric study of adverse pressure gradient turbulent boundary layers. *Int. J. Heat Fluid Flow* **32**, 575–585.

Monty, J. P., Harun, Z. & Marusic, I. 2011*b* A parametric study of adverse pressure gradient turbulent boundary layers. *Int. J. Heat Fluid Flow* **32**, 575–585.

Morrison, Jonathan F, McKeon, B. J., Jiang, W & Smits, A. J. 2004 Scaling of the streamwise velocity component in turbulent pipe flow. *J. Fluid Mech.* **508**, 99–131.

Nagib, H. M., Chauhan, K. A. & Monkewitz, P. A. 2007 Approach to an asymptotic state for zero pressure gradient turbulent boundary layers. *Phil. Trans. R. Soc.* **365**, 755–770.

Nickels, T. B. 2004 Inner scaling for wall-bounded flows subject to large pressure gradients. *J. Fluid Mech.* **521**, 217–239.

Örlü, R., Fransson, J. H. M. & Alfredsson, P. H. 2010 On near wall measurements of wall bounded flows — the necessity of an accurate determination of the wall position. *Prog. Aero. Sci.* **46**, 353–387.

Örlü, R. & Schlatter, P. 2013 Comparison of experiments and simulations for zero pressure gradient turbulent boundary layers at moderate Reynolds numbers. *Exp. Fluids* **54**, 1547.

Örlü, R., Segalini, A., Klewicki, J. & Alfredsson, P. H. 2016 High-order generalisation of the diagnostic scaling for turbulent boundary layers. *J. Turbulence* **17**, 664–677.

Örlü, R. & Vinuesa, R. 2017 Thermal anemomentry. In *Experimental Aerodynamics* (ed. S. Discetti & A. Ianiro). CRC Press.

Österlund, J. M. 1999 Experimental studies of zero pressure-gradient turbulent boundary layer flow. *Ph. D. thesis, Royal Institute of Technology, Stockholm, Sweden* .

Rodríguez-López, E., Bruce, P. J. K. & Buxton, O. R. H. 2015 A robust post-processing method to determine skin friction in turbulent boundary layers from the velocity profile. *Exp. Fluids* **56**, 68–16.

Rodríguez-López, E., Bruce, P. J. K. & Buxton, O. R. H. 2016 On the formation mechanisms of artificially generated high Reynolds number turbulent boundary layers. *Boundary-Layer Meteor.* **160**, 201–224.

Schlatter, P. & Örlü, R. 2010 Assessment of direct numerical simulation data of turbulent boundary layers. *J. Fluid Mech.* **659**, 116–126.

Schlatter, P. & Örlü, R. 2012 Turbulent boundary layers at moderate reynolds numbers: inflow length and tripping effects. *J. Fluid Mech.* **710**, 5–34.

Sillero, J. A., Jiménez, J. & Moser, R. D 2013 One-point statistics for turbulent wall-bounded flows at Reynolds numbers up to $\delta^+ \simeq 2000$. *Phys. Fluids* **25**, 105102.

Simens, M., Jiménez, J., Hoyas, S. & Mizuno, Y. 2009 A high-resolution code for turbulent boundary layers. *J. Comput. Phys.* **228**, 4218–4231.

Tang, Z., Jiang, N., Zheng, X. & Wu, Y. 2016 Bursting process of large- and small-scale structures in turbulent boundary layer perturbed by a cylinder roughness element. *Exp. Fluids* **57**, 79.

Tani, I. 1969 Boundary-layer transition. *Annu. Rev. Fluid Mech.* **1**, 169–196.

Vincenti, P., Klewicki, J., Morrill-Winter, C., White, C. M. & Wosnik, M. 2013 Streamwise velocity statistics in turbulent boundary layers that spatially develop to high reynolds number. *Exp. Fluids* **54**, 1629.

Vinuesa, R., Bobke, A, Örlü, R. & Schlatter, P. 2016*a* On determining characteristic length scales in pressure-gradient turbulent boundary layers. *Phys. Fluids* **28**, 055101.

Vinuesa, R., Duncan, R. D. & Nagib, H, M. 2016*b* Alternative interpretation of the Superpipe data and motivation for CICLoPE: The effect of a decreasing viscous length scale. *Eur. J. Mech. B/Fluids* **58**, 109–116.

Vinuesa, R. & Örlü, R. 2017 Measurement of wall shear stress. In *Experimental Aerodynamics* (ed. S. Discetti & A. Ianiro). CRC Press.

Vinuesa, R., Rozier, P. H., Schlatter, P. & Nagib, H. M. 2014 Experiments and computations of localized pressure gradients with different history effects. *AIAA J.* **52**, 368–384.

Wu, X, Moin, P. & Hickey, J.-P. 2014 Boundary layer bypass transition. *Phys. Fluids* **26**, 091104.